Paleomagnetic data from the Rinconada fault in central California: Evidence for off-fault deformation

Sarah E. Crump
Senior Integrative Exercise
March 10, 2010

Submitted in partial fulfillment of the requirements for a Bachelor of Arts degree from Carleton College, Northfield, Minnesota.

Table of Contents

Paleomagnetic data from the Rinconada fault in central California: Evidence for off-fault deformation

Sarah E. Crump
Carleton College
Senior Integrative Exercise
March 10, 2010

Advisor: Sarah Titus

ABSTRACT

Paleomagnetic data can be used to understand the distribution of off-fault deformation in actively deforming plate boundaries such as the San Andreas fault. Although large clockwise vertical axis rotation from paleomagnetic data have been documented in California since the 1980s, it has typically been assumed that rotations ceased immediately north of the western Transverse Ranges. However, this study documents small but significant rotations north of the western Transverse Ranges along the Rinconada fault in central California.

Samples were collected from 177 sites in the Miocene Monterey Formation for paleomagnetic analysis. For the 58 statistically viable sites, the average clockwise rotation is 8.4º ± 7.9º. Because stations may be located on different fault blocks, it is also important to examine spatial patterns of rotations along and across the fault. In the north, clockwise rotations were as high as ~25º; in the central and southern portions, there are regions with no appreciable rotation, moderate (10º-22º) clockwise rotation, and even several stations with ~15º counterclockwise rotations, which is an unexpected result for a dominantly dextral fault system.

Comparison of these paleomagnetic results with rotations computed from two independent predictors of bulk rotation—from fold patterns and from a GPS velocity field—provides insight into the spatial patterns of rotation in the area, suggesting that off-fault deformation is controlled in part by 1) basement rock types and 2) the creeping-to-locked transition on the San Andreas fault. It is important to characterize the style and magnitude of off-fault deformation from data sets such as paleomagnetic rotations because the distribution of plate boundary deformation is reflected in seismicity; thus, accurate kinematic models and earthquake hazard forecasting can improve with a more complete understanding of distributed deformation.

Keywords: Central California; San Andreas fault; Paleomagnetism; Transpression; Transform faults

INTRODUCTION

Plate boundary zones are often complex regions of deformation that are tens to hundreds of kilometers wide. In these regions, faults typically receive the most attention because of the seismic hazards they present. For example, many studies have focused on the San Andreas fault in California because of the destruction from earthquakes such as the 1906 San Francisco and 1989 Loma Prieta earthquakes (e.g. Rubinstein and Beroza, 2004; Wells, 2004; Boatwright and Keefer, 2005; Twiss and Unruh, 2007; Olsen et al., 2008; Aagaard et al., 2009). However, this fault-centric view leads to an incomplete description of plate boundary deformation if off-fault structures are not accurately characterized. In California, plate boundary deformation is known to be distributed away from major strike-slip faults in the San Andreas fault system; for example, distributed deformation accounts for the uplift and deformation of the Coast Ranges. To better understand these complex plate boundary systems and their potential for destructive seismicity, we must better characterize how deformation is accommodated on faults and in their borderlands.

This study is focused on characterizing off-fault deformation in central California. The southern part of the region—the westernTransverse Ranges—is perhaps the best known example of significant off-fault deformation in California. Here, large (~90º) clockwise rotations have been documented in internally rigid crustal blocks (Luyendyk et al. 1985, Hornafius et al. 1986). Because the pioneering work of Luyendyk et al. (1985) showed no rotation immediately north of the Big Pine fault, most workers have assumed that no rotation has occurred in the rest of central California. However, results of narrowly-focused studies from sites near the Rinconada fault found small (<15º) but not

insignificant clockwise rotations (Omarzai, 1996; Titus et al., 2007), suggesting that further investigation of vertical axis rotations in central California is needed.

In this study, I use paleomagnetic data from the Miocene Monterey Formation along much of the Rinconada fault to document off-fault deformation north of the Transverse Ranges and adjacent to the creeping segment of the San Andreas fault. This region is ideal for study because (1) the geometry of the system is simpler: the Rinconada fault is straight and parallel to its more important cousin—the San Andreas fault; (2) the Monterey Formation is widespread in central California and is commonly used in paleomagnetic studies, including those from the western Transverse Ranges; (3) the Monterey Formation was deposited after passage of the Mendocino Triple Junction in this region, meaning that any rotations recorded by paleomagnetism in these rocks is related to the San Andreas fault system. In this paper, I lay out the geologic and tectonic setting that control deformation in central California. I then present the results of this paleomagnetic study along with comparisons of the paleomagnetic rotations with independent calculations of rotation from two other data sets. Finally, I propose geologic and kinematic explanations for the spatial patterns of rotation in central California and emphasize the importance of incorporating off-fault deformation into kinematic modeling and seismic forecasting.

GEOLOGIC SETTING

Tectonic Setting

The most prominent example of documenting off-fault deformation in central California from paleomagnetic data comes from the western Transverse Ranges, an east-

west oriented set of mountain ranges that are now offset along the "Big Bend" section of the San Andreas fault (Fig. 1), where relative plate motion is ~20º oblique to the fault strike. Paleomagnetic data show that ~100-km-long blocks in the western Transverse Ranges have rotated up to 95º clockwise since the early Miocene (Luyendyk et al., 1980; Hornafius et al., 1986). These studies also suggest that no significant vertical axis rotation has occurred north of the sinistral Big Pine fault that bounds the northern margin of the range.

Other paleomagnetic data from north of the Western Transverse Ranges provide somewhat conflicting evidence for vertical axis rotations. Terres (1984) and Onderdonk (2005) each found small rotations in both clockwise and counterclockwise directions, implying that no appreciable rotation had occurred. However, Ellis (1994) documented consistent clockwise rotations of ~23º in the Cuyama basin. Larger (~40-60º) clockwise rotations have been documented at several sites along the coast in central California (e.g. Greenhaus and Cox, 1979; Holm et al., 1991; Horns and Verosub, 1995). Along the Rinconada fault, the focus area of this study, Omarzai (1996) and Titus (2007) both found ~15º of clockwise rotation. Together, these data sets suggest that central California has experienced a complex history of vertical axis rotation.

In this study, I focus on a larger region north of the western Transverse Ranges in central California. This area includes the creeping segment of the San Andreas fault, which slips aseismically between San Juan Bautista and Cholame (Fig. 2). Slip rates along the creeping segment are 28-30 mm/yr (Burford and Harsh, 1980; Titus et al., 2005) and decrease toward the locked sections to the northwest and southeast, which last ruptured in the 1906 San Francisco and 1857 Fort Tejon earthquakes, respectively. The

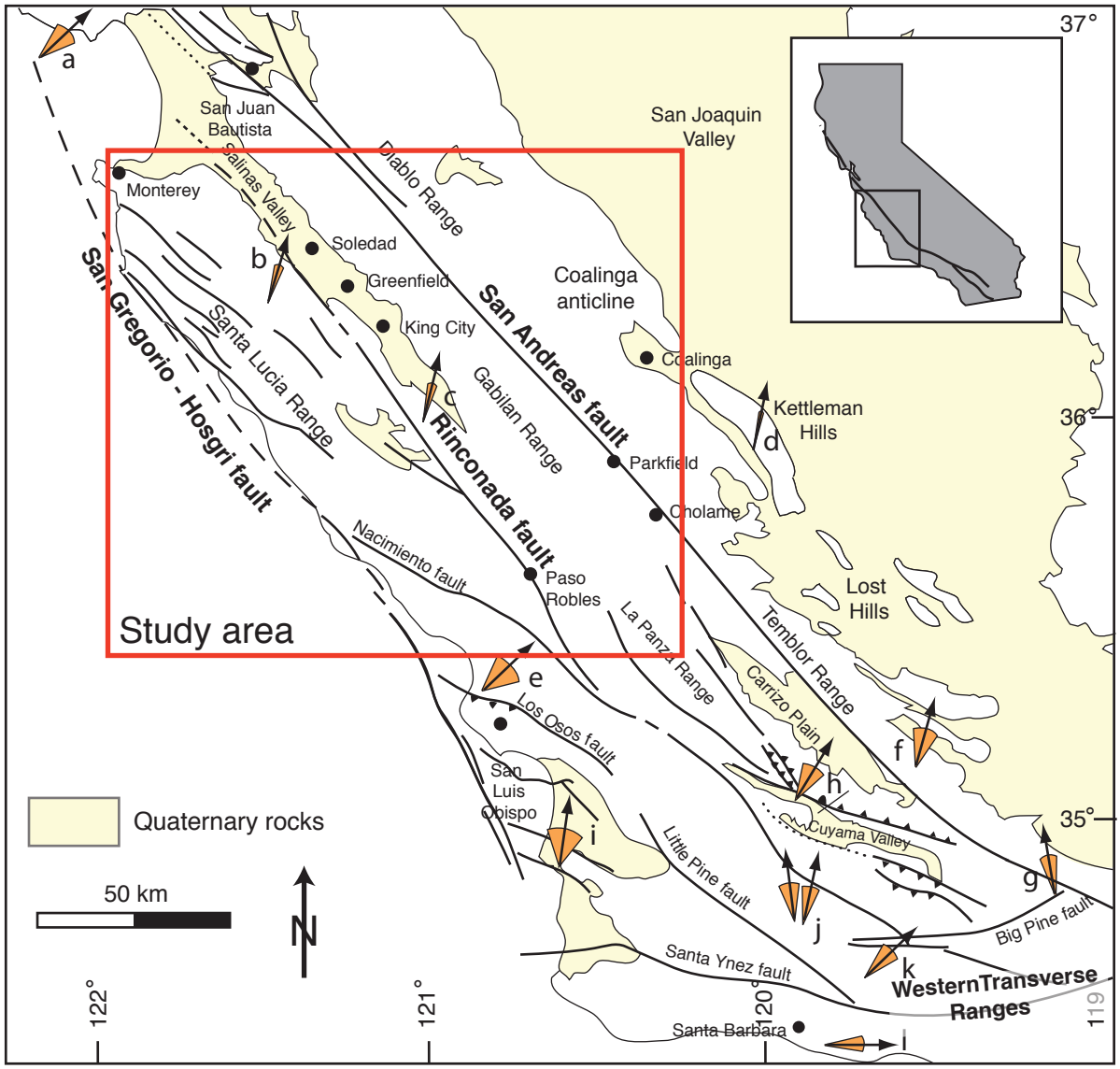

Figure 1. Map of central California showing major faults, topographic features, cities, and paleomagnetic rotation vectors (with orange error wedges) from previous studies. The region from which paleomagnetic data were collected for this study is outlined by the red box. Paleomagnetic data: a.) Clockwise rotations of 35-55º near Santa Cruz (Holm et al., 1991); b.) clockwise rotations 14±5º from near Greenfield (Omarzai, 1996); c.) clockwise rotation of 14±7º from preliminary data in this study area (Titus et al., 2007); d.) clockwise rotation of 12±2º in Kettleman Hills (White, 1987); e.) clockwise rotations of 49º near Morro Bay (Greenhaus and Cox, 1979); f., g.) mean clockwise rotation of 6.4º in Lockwood Valley (Terres, 1984); h.) clockwise rotation of ~23º in Cuyama basin (Ellis et al. 1993); i.) no significant rotation at Lions Head (Luyendyk et al. 1985); j.) no significant rotations at Figueroa Mountain (Onderdonk, 2005); k.) clockwise rotations of 40º near western Big Pine Fault (Onderdonk, 2005); l.) clockwise rotation of ~90º in the Western Transverse Ranges (Luyendyk et al., 1985). Map modified from Page et al. (1998).

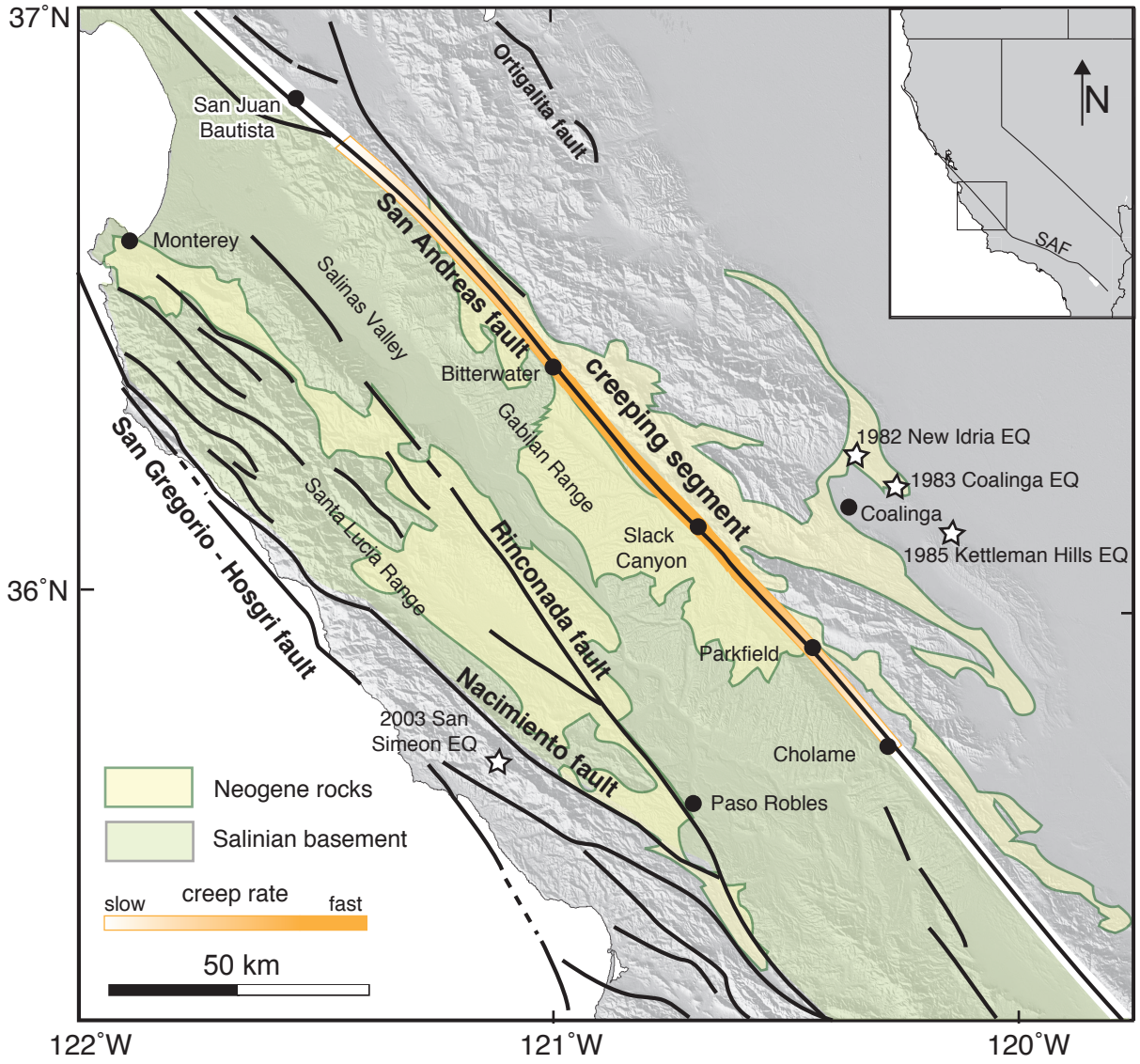

Figure 2. Digital elevation map of central California highlighting the Salinian block (in green), the creeping segment of the San Andreas fault (in orange), and recent off-fault earthquakes. Note that creep rate is highest between Bitterwater and Parkfield, adjacent to the Rinconada fault study area. Modified from Titus et al. (in revew).

fastest slip rates on the creeping segment are still slower than the expected fault-parallel component of relative plate motion of 37-39 mm/yr (Argus and Gordon, 2001; d'Alessio et al., 2005; Titus et al., 2006); this missing motion must be accommodated somewhere else in the plate boundary system. Bird (2009) estimates a rate of total distributed deformation of 2.6 mm/yr, or about 7-13% of plate motion, in this section of the fault system. My analysis of off-fault rotations is thus particularly important in further understanding how permanent deformation is distributed across a broad fault zone.

Rinconada fault

The 250-km-long Rinconada fault system is one of three major sub-parallel faults of the San Andreas fault system in central California. Since the Tertiary, ~60 km of slip on the Rinconada fault has been documented, with 18 km of offset occurring since the Pliocene (Dibblee, 1976). Discrete dextral offset on the Rinconada fault accounts for ~1 mm/yr of the fault-parallel component of relative plate motion (Rolandone et al., 2008; Bird, 2009). A well-developed fold and thrust belt flank both sides of the fault.

The paleomagetic data for this study was compiled from the Miocene Monterey Formation, a marine sedimentary unit that includes shales, mudstones, marlstones, dolomites, cherts, and diatomaceous rocks. These rocks were deposited in basins along coastal California and now have widespread exposures in central and southern California (Isaacs, 1981). Previous studies have shown that the Monterey Formation, in particular the dolomitic strata, carries a well-preserved primary remanent magnetization (e.g. Hornafius et al., 1981). Further, the deposition of these rocks after initiation of the San Andreas fault (Blake et al., 1978) make them an ideal recorder of deformation related to the San Andreas fault system.

In the study area along the Rinconada fault, Neogene sedimentary rocks are underlain by a granitic and metasedimentary basement known as the Salinian block (Fig. 2). The granitic plutons and schists of the Salinian block form relatively competent crustal blocks. The Salinian block is interpreted to have formed the southern extent of the Sierra Nevada Batholith and has therefore been translated hundreds of kilometers along faults in the San Andreas fault system to bring it to central California (e.g. Hill and Dibblee, 1953; Champion et al., 1984). On the northeast side of the San Andreas fault, basement types include the greywhacke, shale, limestone, volcanic rocks, and metamorphic rocks of the Franciscan complex. The basement rocks of this mélange belt are significantly less competent than the Salinian block on the southwest side of the fault.

PALEOMAGNETISM

Background

Paleomagnetism relies on ferromagnetic minerals, such as magnetite, ilmenite, and hematite, that can record the direction of the Earth's magnetic field. The resulting magnetic signal locked in rocks, called natural remanent magnetization (NRM), includes the primary NRM, or the direction of the magnetic field when the rock was first acquiring its magnetization, and secondary NRM, components that are acquired later due to physical and chemical processes. The primary NRM acquired by sedimentary rocks, including those used in this study, is a result of detrital remanent magnetization (DRM). This process involves the preferential orientation of ferromagnetic minerals during deposition and lithification due to the ambient magnetic field. Measuring the primary

NRM in a rock can provide useful information on the movement of that rock since its magnetization was acquired.

A magnetic signal is usually represented by a vector that has two components, one vertical and one horizontal. The vertical component, or inclination, is defined as the angle between horizontal and the magnetic field vector and varies from –90º to 90º, where negative values reflect reverse-polarity magnetizations in the northern hemisphere. The horizontal component, or declination, is an azimuthal angle relative to north and varies from 0º to 360º (Fig. 3). Declinations and inclinations are considered anomalous if they do not correlate to the paleomagnetic pole at the time of formation for the *in situ* position of the rock. Inclination anomalies are often interpreted to reflect latitudinal translation of the rock, while declination anomalies suggest rotation about a vertical axis (Fig. 4). I use declination anomalies in this study to examine off-fault deformation in central California.

Methodology

Samples of the Monterey Formation were collected from 177 sites adjacent to the Rinconada fault in central California. Nearly all sites are within 15 km of the fault trace. At each site, 7 to 10 oriented cores were collected. Samples were usually taken in mudstones, siltstones, and dolostones where bedding attitude could be measured accurately.

Cores were cut into 1-6 individual one-inch specimens for analysis. To isolate the primary NRM in each specimen, I used thermal demagnetization. This method involves removing magnetic signals gradually by submitting samples to progressively hotter temperatures up to the Curie temperature (the temperature above which ferromagnetic properties no longer exist) of the main magnetic mineral. I baked specimens starting at

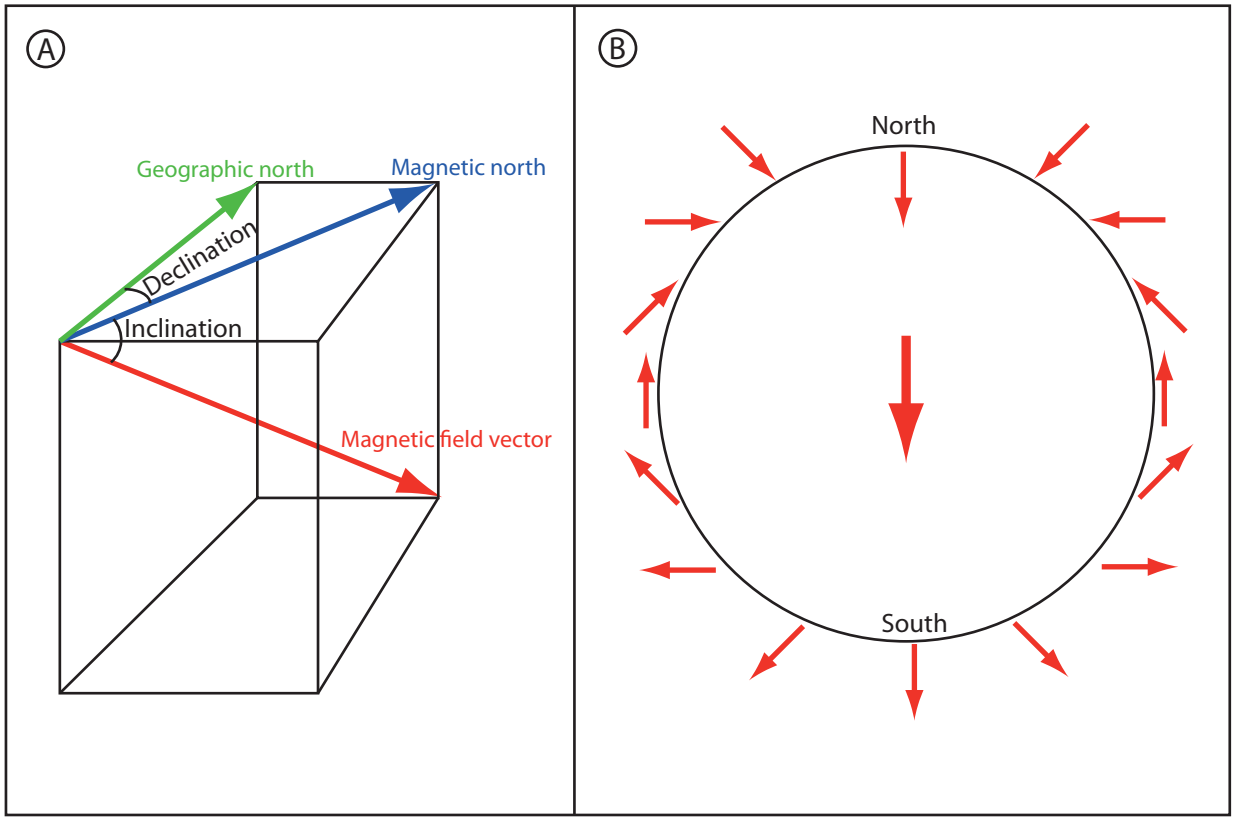

Figure 3. A.) Three-dimensional diagram of declination and inclination. Declination is defined as the angle between geographic north (in green) and magnetic north (in blue) on a horizontal plane. Inclination is the angle between horizontal plane and the magnetic field vector (in red). B.) Cross-section of the Earth taken parallel to the geomagnetic pole (represented by the large red arrow). Small red arrows show expected inclination angles at different latitudes during normal polarity.

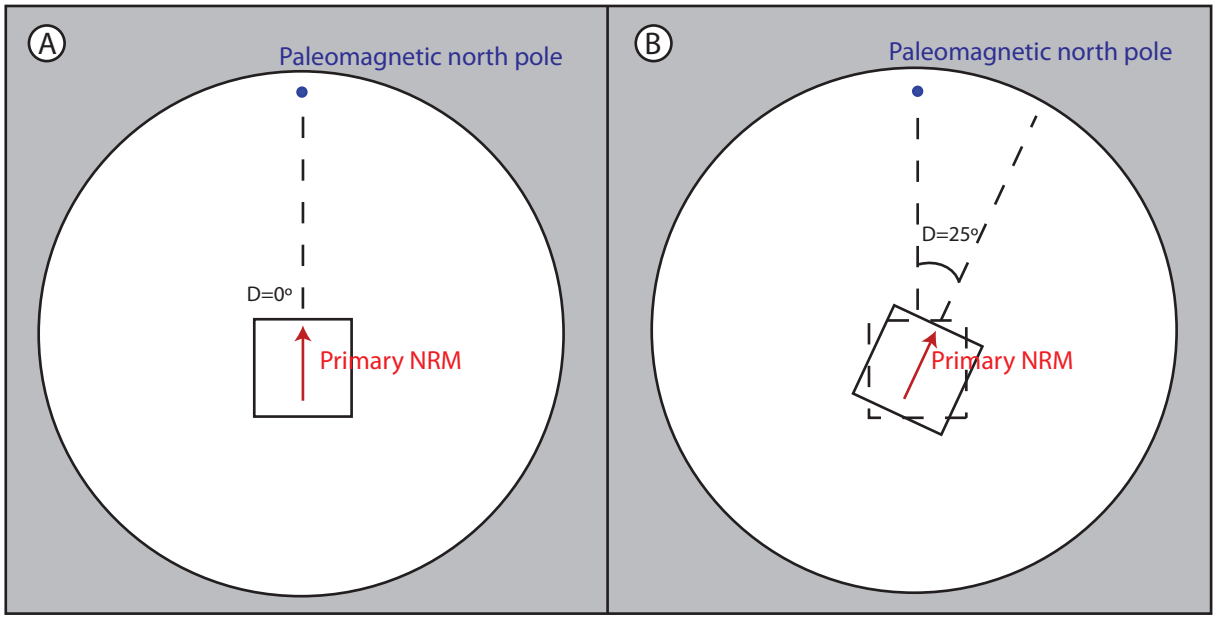

Figure 4. Schematic depiction of how paleomagnetism is used to document vertical axis rotations. The white circles represent the Earth in plan view. A.) At the time that a rock (represented by the square) acquires a natural remanent magnetization (NRM; represented by red arrow) from the geomagnetic field, the declination (D) of that NRM is in line with the magnetic north pole. B.) If the rock rotates through time, the declination of the primary NRM is deflected from the paleopole. That anomaly, which is 25º clockwise in this example, should be equivalent to the amount of vertical axis rotation experienced by the rock.

80ºC and increased up to ~550ºC by 20-25º increments. Between each thermal step, the magnetic moment was measured in a cryogenic magnetometer and sensed by a superconducting quantum interference device (SQUID) for eight orientations of the specimen. Specimens were measured and stored in a field-free room so as to minimize remagnetization during processing. All measurements were made in the Pacific Northwest Paleomagnetism Laboratory at Western Washington University.

The primary NRM can be identified by analyzing the step-wise removal of progressively higher-stability components in a given specimen. I analyzed demagnetization paths using the in-house CryoThing Analysis program. Anchored best-fit lines were calculated on Zijderveld projections (Zijderveld, 1967) for each specimen after demagnetization was complete. Because many specimens had weak magnetic signals and were often remagnetized during the demagnetization process, I was unable to interpret reliable demagnetization paths for many of the specimens.

After fitting one or more anchored lines to the demagnetization path, I assigned a letter grade of A-F to the Zijderveld diagrams based on visual scatter and mean angular deviation. Figure 5 shows representative Zijderveld diagrams for this grading system. Site means were calculated for sites with at least three specimens whose best-fit line yielded an angular 95% confidence of <15º. The declination and inclination of specimens with reverse-polarity signals were inverted for averaging.

I compared the site means to the North American Miocene paleopole (Besse & Courtillot, 2002) to compute declination anomalies. Rotations and their errors were calculated using the methods outlined in Demarest (1983). I included site means whose declination yielded a 95% confidence ellipse of <20º in the results. To examine the

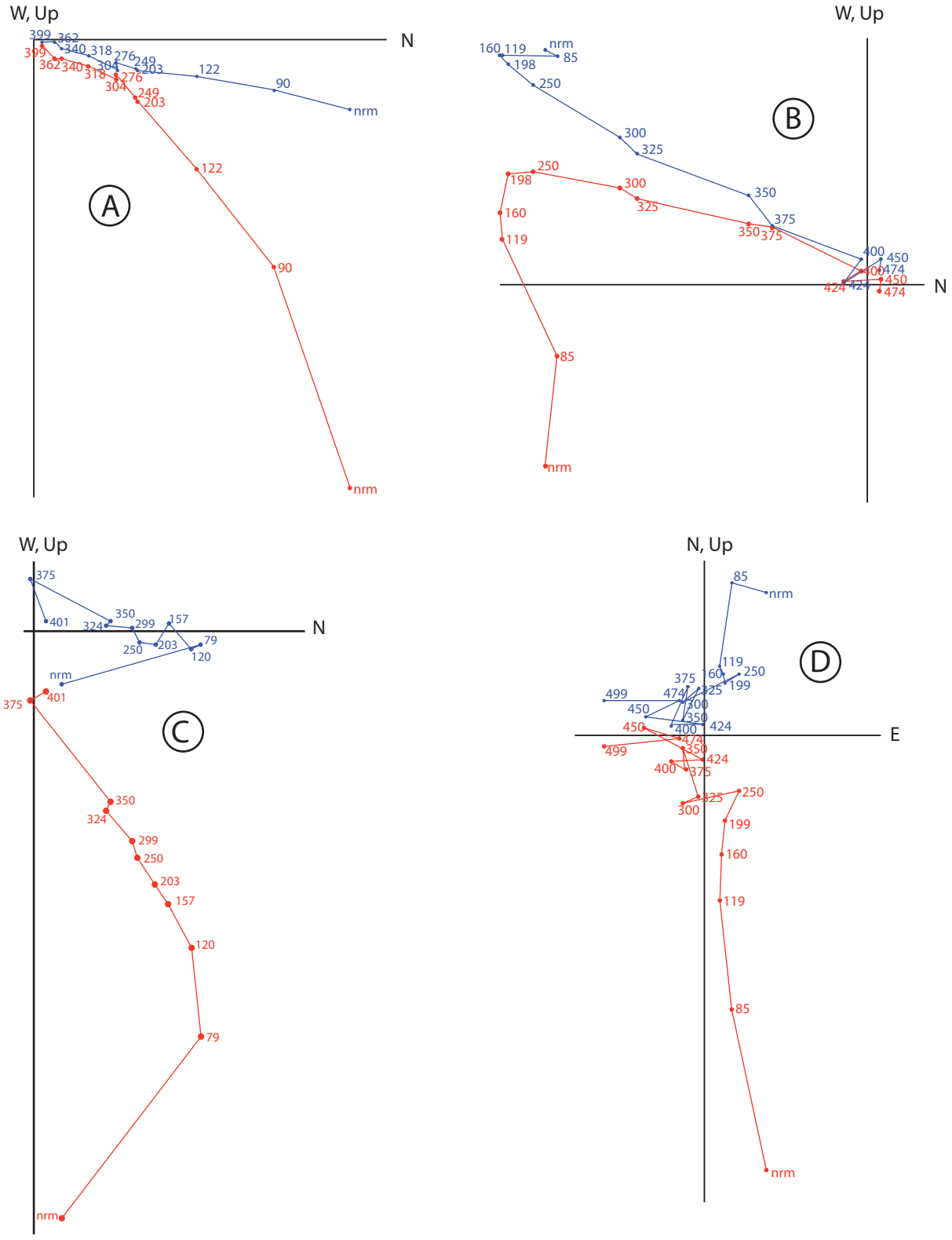

Figure 5. Representative Zijderveld diagrams for the grading system used to select data. Red points and lines represent inclination, and blue points/lines represent declination. Numbers indicate the temperature (in ºC) for that thermal step. A.) Specimen 88-3b: grade A normal polarity demagnetization path; B.) specimen 124-5b: grade B reverse polarity demagnetization path; C.) specimen 126-7: grade C normal polarity demagnetization path; D.) specimen 123-2c: grade D normal polarity demagnetization path that exhibits remagnetization. Specimens assigned a grade of F show no systematic demagnetization path.

spatial patterns of deformation, I divided the region into five distinct geographical subgroups: Arroyo Seco, Lockwood, San Antonio Reservoir, Paso Robles, and Indian Valley. From the site mean rotations, I also calculated local means (averages of 2-8 adjacent sites) to determine a lower-resolution but more statistically robust estimate of rotations. Local means with a concentration parameter (k) of greater than 10 were included in the results. Results are reported in Tables 1 and 2 and on maps in Figures 6 and 7. Note that rotation error wedges are not shown for the site means in Figure 6 in order to preserve clarity. Although local means have relatively large rotation errors due to small sample sizes, these averages represent more reliable rotations than the site means.

Reversal and Tilt Tests

Of the 58 statistically viable sites, 11 record reverse-polarity signals. All 11 reverse sites pass reversal tests (Fig. 8), indicating that the isolated signal was indeed primary and that the samples provide a reliable average of geomagnetic secular variation.

Taken together, the 58 sites fail a Tauxe and Watson (1994) tilt test with maximum clustering at ~50% untilting (Fig. 9a). Generally, a failed tilt test indicates that the isolated signal was actually acquired during folding. However, there are several reasons why the samples probably do record the primary NRM. First, tilt corrections do not take into account the plunge of the folds, so fold orientation may have resulted in dispersion in the tilt-corrected data. Second, because samples were taken from a large spatial area and represent a range of rotational magnitudes, they may not cluster well as a group. Third, and most important, the 11 reverse-polarity samples pass the tilt test at 100% untilting (Fig. 9b). This is probably because the primary signal in reverse-polarity samples is more easily distinguished from secondary present-day signals, so best-fit lines

Site	Declination	Inclination	k	N	α95	Rotation (º)	Rotation error (± º)
1	3.2	53.3	176.0	7	4.6	9.7	8.2
2	10.8	54.2	30.2	5	14.1	6.0	20.0
6	39.6	87.5	44.0	6	10.2	34.8	55.0
7	15.2	1.1	103.0	4	9.1	22.0	9.0
8	29.3	28.1	62.1	6	8.6	35.8	9.5
10	12.7	13.2	36.6	4	15.4	7.8	13.1
14	7.0	22.1	107.3	5	7.4	13.6	7.1
16	4.8	55.1	43.9	6	10.2	11.5	14.8
17	355.0	56.3	333.4	6	3.7	-9.8	6.2
20	358.2	47.9	142.9	6	5.6	4.8	7.4
21	14.6	45.3	206.0	6	4.7	21.2	6.2
22	16.5	32.0	222.3	6	4.5	23.1	5.3
23	31.6	48.5	117.6	6	6.2	38.2	8.1
25	356.2	60.2	203.1	7	4.2	-8.6	7.5
26	4.6	62.7	64.4	6	8.4	11.2	15.2
29	327.6	43.0	20.2	5	17.5	-37.2	19.7
31	40.7	3.6	19.0	7	14.2	35.9	11.8
42	356.5	14.1	26.3	6	13.3	3.1	11.4
44	5.2	46.7	30.0	6	12.4	0.4	15.0
46	344.2	42.9	24.2	5	15.9	-9.2	17.8
47	338.2	59.2	18.1	5	18.5	-26.6	30.8
50	296.4	63.1	54.8	4	12.5	-68.4	23.1
52	54.2	446.0	114.7	3	11.6	49.4	13.8
58	342.7	65.1	193.4	6	4.8	-11.8	10.1
60	35.8	22.8	49.8	6	9.6	42.4	8.9
61	6.9	30.0	122.3	6	6.1	2.1	6.5
62	25.0	18.5	68.2	5	9.3	31.6	8.5
63	352.3	57.7	171.7	7	4.6	-1.1	6.3
65	1.4	-1.4	96.7	7	6.2	8.0	5.9
66	47.5	45.1	88.7	6	7.2	54.1	8.8
68	22.4	18.6	118.0	3	11.4	17.6	10.2
72	345.1	-1.6	70.8	3	14.8	-19.7	12.3
74	5.8	9.9	42.4	3	19.2	1.0	15.9
77	25.2	3.3	63.1	3	15.6	20.4	12.9
80	358.2	26.9	42.8	3	17.1	-6.6	15.7
82	23.4	58.0	80.2	3	13.9	18.6	21.8
88	41.3	30.2	154.6	3	9.9	36.5	9.7
90	355.9	15.7	36.2	3	20.8	-8.9	17.6
118	359.8	50.2	319.3	3	6.9	-5.0	9.2
120	356.8	53.7	408.8	3	6.1	-8.0	8.9
121	11.3	55.5	749.8	3	4.5	6.5	7.2
122	357.3	49.6	325.6	3	6.8	-7.5	9.0
124	41.0	-41.4	126.3	3	11.0	36.2	12.2
125	48.0	53.7	889.0	6	2.2	43.2	4.4
130	29.5	62.5	550.9	5	3.3	24.7	6.6
132	49.1	45.5	98.7	6	6.8	44.3	8.4
133	21.8	7.3	169.8	3	9.5	17.0	8.3
135	13.6	37.2	58.7	3	16.2	8.8	16.7
138	19.4	44.5	57.3	4	12.2	14.6	14.2
140	1.0	53.1	239.2	5	2.2	-3.8	4.4
141	22.1	49.8	186.6	4	6.7	17.3	8.9
154	38.1	34.8	41.2	3	19.4	33.3	19.4
158	31.4	44.2	49.4	7	8.7	26.5	10.3
160	3.1	68.1	33.3	6	11.8	-1.8	26.8
162	1.8	46.0	157.6	3	9.9	-3.1	11.9
169	340.1	55.0	90.4	3	13.0	-24.7	18.8
170	349.2	60.3	117.1	4	8.5	-15.6	14.3
177	44.8	33.8	43.9	4	14.0	40.0	13.9

Table 1. Results for all used paleomagnetic sites. **k** is a concentration parameter; **N** is the number of specimens used to calculate site mean; **α95** is the 95% confidence ellipse; positive rotations are clockwise.

Sites included	Declination	Inclination	k	N	α95	Rotation	Rotation error
1, 2, 6	358.6	74.4	18.8	3	19.3	-6.2	41.0
60, 120, 121, 177	30.2	41.4	15.2	4	20.3	25.4	22.3
7, 8, 14, 61-63, 65, 66	15.2	24.7	12.3	8	16.4	10.4	14.8
77, 122, 125, 138, 140	18.6	42.6	10.4	5	24.9	13.8	28.1
20-23, 88	17.5	52.0	89.7	5	8.1	12.7	11.1
16, 17, 29	347.3	52.6	32.2	3	22.8	-17.5	30.8
158, 162	9.3	52.7	21.4	2	27.3	4.4	39.5
80, 82, 154	18.8	41.2	12.6	3	36.3	14.0	41.6
130, 132, 133, 135	27.2	19.1	10.0	4	30.6	22.4	32.9
25, 26, 42, 44, 47, 50	349.8	53.3	20.2	6	12.0	-15.0	28.4

Table 2. Results for local means calculated from multiple adjacent site means. **k** is a concentration parameter; **N** is the number of sites used to calculate local mean; **α95** is the 95% confidence ellipse; positive rotations are clockwise.

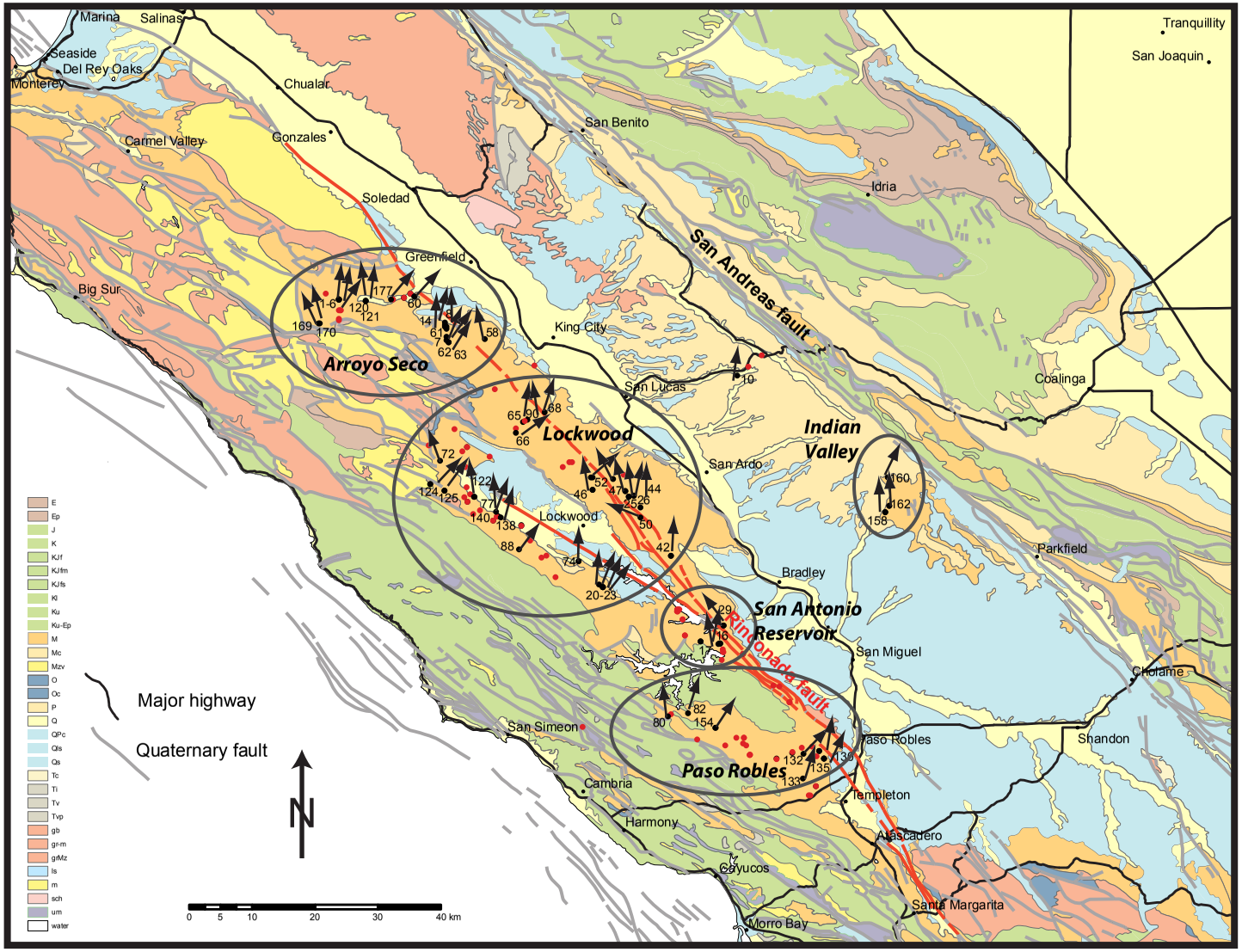

Figure 6. Geologic map of study area with site mean paleomagnetic rotations shown as vectors whose angular deviation from north represents rotational magnitude and direction. Black numbers and dots correspond to used sites; red dots correspond to sites that were not used due to unreliable data. Error wedges are not included for the sake of clarity.

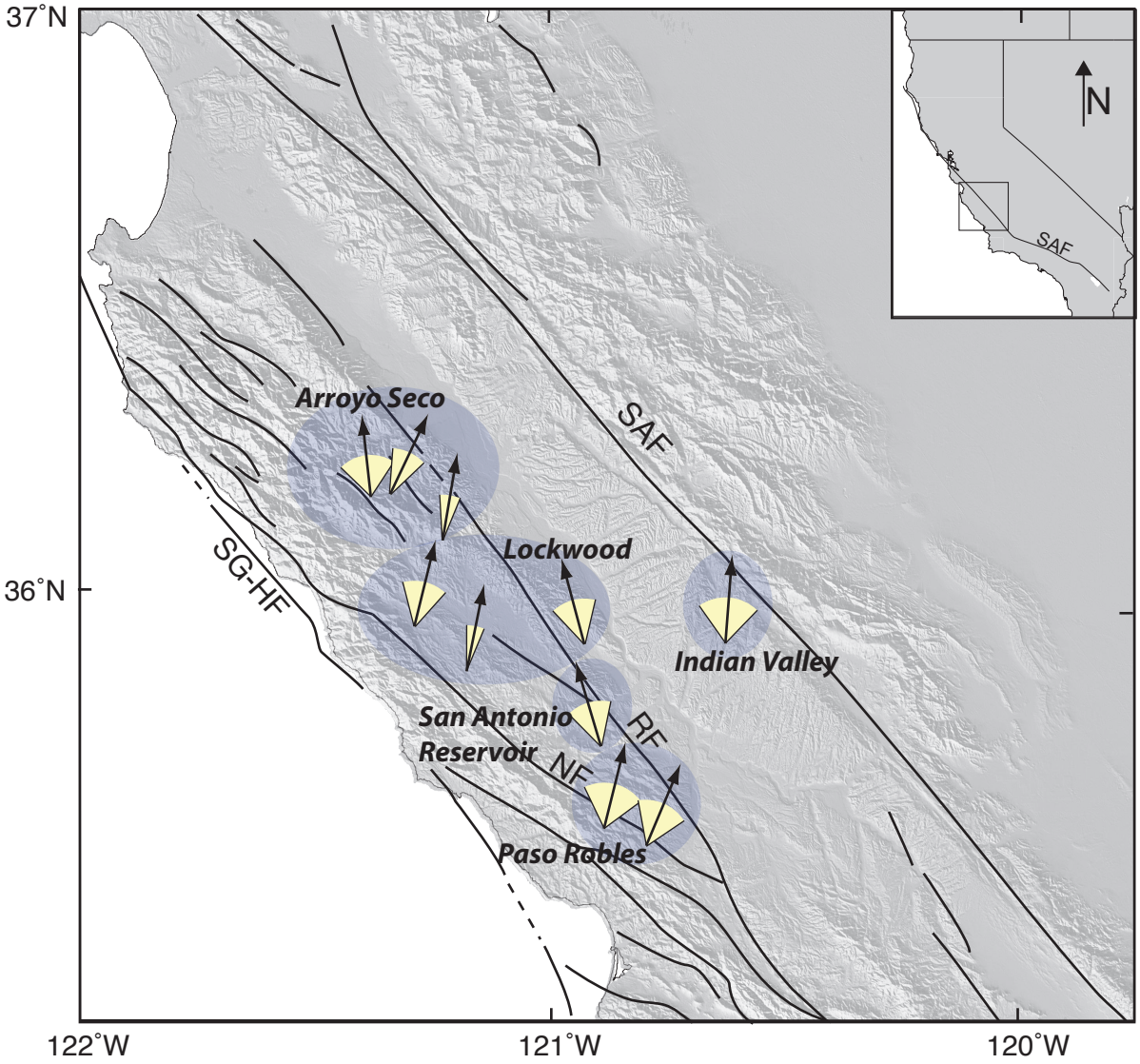

Figure 7. Local paleomagnetic rotation means, averaged from multiple adjacent site means, on a topographic map of central California. Yellow wedges indicate angular rotation errors. Subgroups are labeled and highlighted by blue ellipses. SAF = San Andreas fault; SG-HF = San Gregorio-Hosgri fault; RF = Rinconada fault; NF = Nacimiento fault.

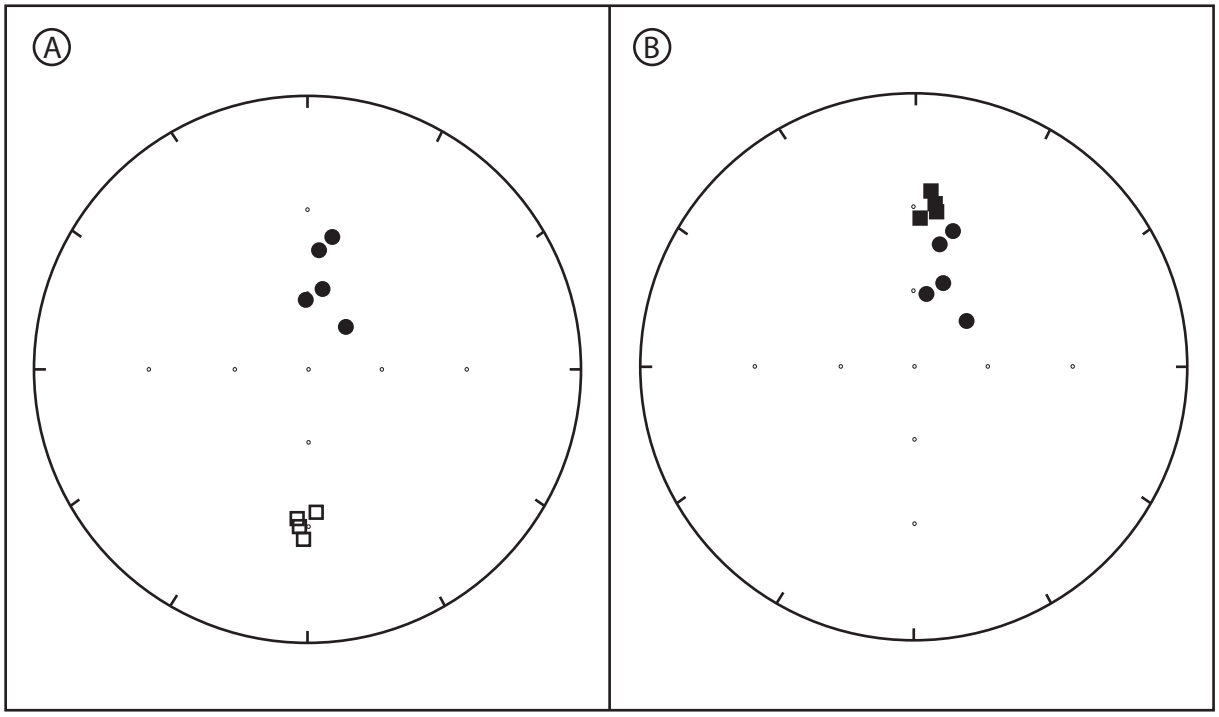

Figure 8. Representative reversal test plotted in equal-area stereonets. A.) Primary natural remanent magnetization data from two adjacent sites (circles from site 2; squares from site 120). B.) When reverse-polarity signals (open symbols in A) are inverted through the origin, they fall within the range of the normal-polarity signals (closed symbols). Data from the 11 used reverse-polarity sites pass this reveral test, indicating that the magnetic signal recorded is indeed primary and can be used to measure vertical axis rotations.

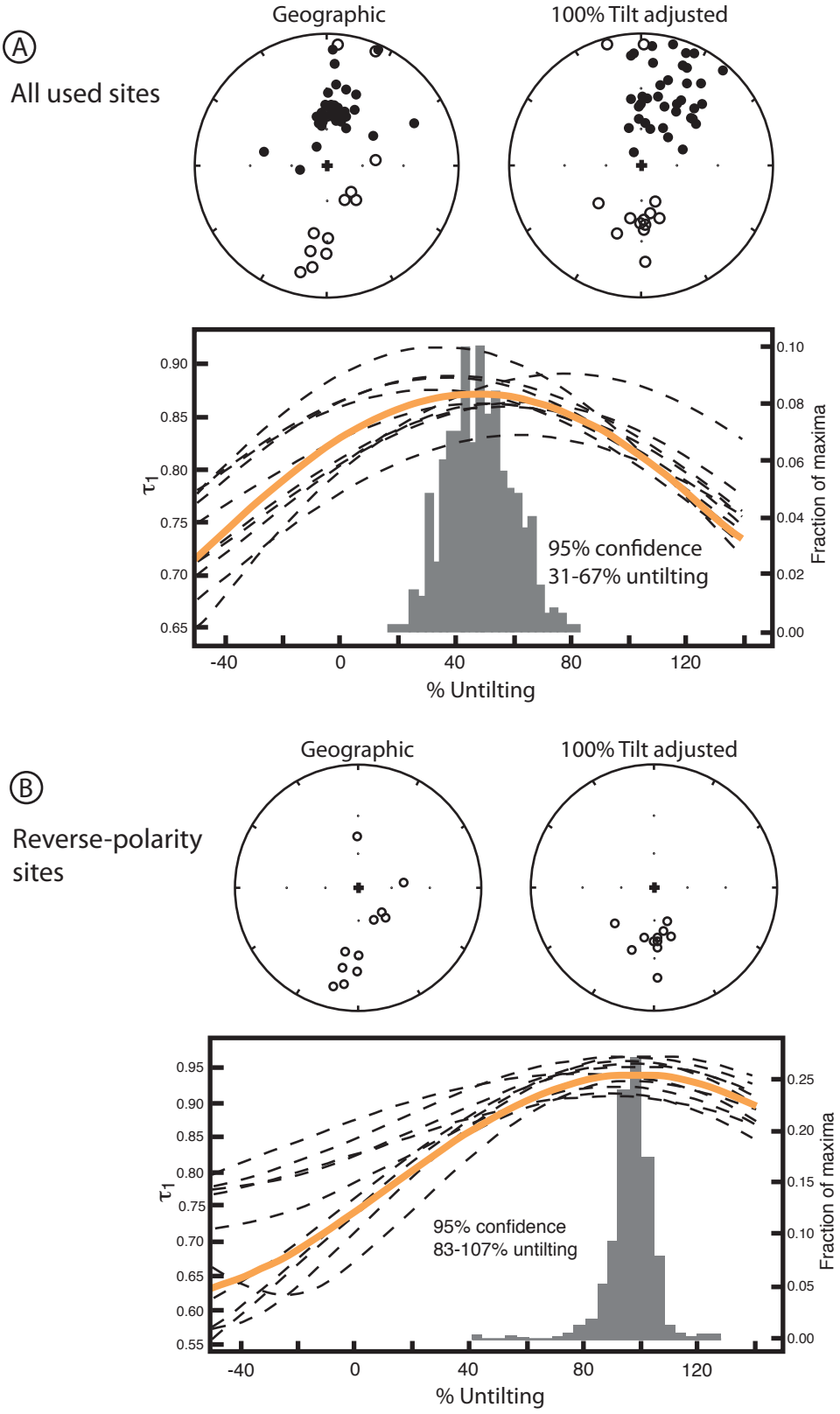

Figure 9. Results of the Tauxe and Watson (1994) paleomagnetic tilt test for all 58 used sites (A) and for the 11 used reverse-polarity sites (B). Equal-area stereonets show magnetization directions for *in situ* (geographic) positions and after correcting to paleohorizontal (100% tilt adjusted). The test output for all used sites shows maximum clustering at ~50% untilting, suggesting that magnetizations were acquired during folding. However, the reverse-polarity sites show maximum clustering at 100% untilting, suggesting that the signals are actually primary. See text for further exlanation.

are more reliable. The successful tilt test of the reverse-polarity data indicate that all the samples have a primary signal recorded and that 100% tilt-corrected data may safely be used for determining rotations.

Results

The mean rotation for all 58 statistically viable site means is 8.4º ± 7.9º, which seems to indicate no significant rotation. However, because of the reasons discussed above, it may not be appropriate to average the results from the entire study area. Careful examination of the spatial distribution of rotation reveals that significant rotations have indeed occurred in parts of the study area. The magnitude of rotations varies with distance from the Rinconada fault and also along its strike.

Paleomagnetic data from most sites indicate moderate amounts of clockwise rotation. In the Arroyo Seco subgroup, site means display a gradient in clockwise rotations relative to the fault. Sites furthest from the fault show no rotation or even minor counterclockwise rotations, while sites closest to the fault show ~ 25º of rotation. This fault-perpendicular gradient is displayed less convincingly in the Paso Robles subgroup and is absent in other subgroups; this may in part be because no other region has an easily accessible fault-perpendicular area for sampling. Other areas along the southwest side of the Rinconada fault, including most sites within the Lockwood subgroup, consistently display a moderate amount of clockwise rotation (from ~10º to ~22º).

There are a few important instances where data diverge from the clockwise rotation expected for a dextral fault system. Sites within the Indian Valley subgroup, nearest the SAF, show essentially no rotation (local mean of 4.4º ± 39.5º). Two areas along the southern Rinconada fault actually show moderate counterclockwise rotation

(~ -15º)—the San Antonio Reservoir subgroup and sites on the northeast side of the Rinconada fault in the Lockwood subgroup.

COMPARISON WITH OTHER DATA SETS

In order to fully understand the spatial variation of rotations along the Rinconada fault, including regions that exhibit no rotation or counterclockwise rotation, I compare results with two data sets that independently record regional off-fault deformation. This comparison necessarily widens the focus of this study from off-fault deformation along the Rinconada fault to off-fault deformation across the entire central San Andreas fault system. However, analyzing patterns from this broader region helps characterize deformation documented along the Rinconada fault. The comparison involves two data sets from Titus et al. (in review): 1) mapped folds and a simple kinematic model of deformation for measuring long-term geologic deformation; and 2) GPS data that show patterns of off-fault deformation derived from the modern velocity field.

Long-term deformation data

Long-term deformation is characterized from map data, including the orientation of fold hinges and their associated limb dips. As illustrated by Figure 10a, folds in central California are concentrated along the northeast side of the San Andreas and along both sides of the Rinconada fault, with a region of little or no deformation between the faults. These fold-related data are used to create a deformation matrix based on monoclinic transpression (Fossen and Tikoff, 1993). Useful parameters can be calculated from this matrix, including the style of deformation and the predicted paleomagnetic rotations.

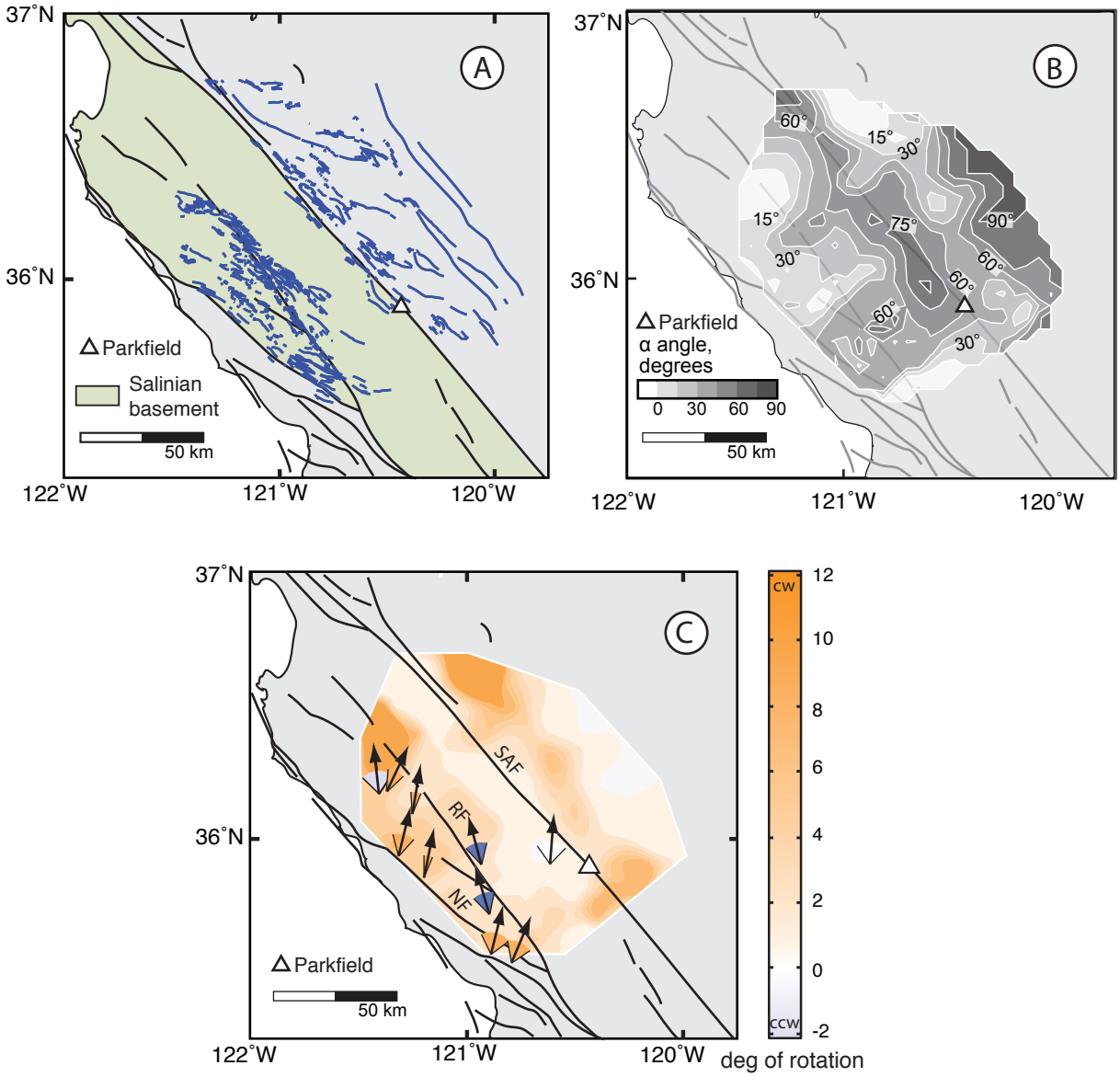

Figure 10. Maps of central California with information based on mapped fold data. A.) Mapped fold hinges; note that little or no deformation has occurred southwest of the San Andreas fault in the Salinian block. B.) Contoured map of the angle of oblique convergence (α) based on fold hinge orientations and limb dips. C.) Contoured plot of rotations predicted from fold data; paleomagnetic local mean rotations are superimposed, with error wedges colored with the same rotation-based color scheme as the contoured plot. SAF = San Andreas fault; RF = Rinconada fault; NF = Nacimiento fault. Modified from Titus et al. (in review).

The style of deformation is characterized by α, the angle of oblique convergence. When $\alpha = 0^{\circ}$, deformation is solely non-coaxial (simple shear); when $\alpha = 90^{\circ}$, deformation is solely coaxial (pure shear); when $0^{\circ} < \alpha < 90^{\circ}$, the style of deformation is transpressional. Oblique convergence angles are calculated on a 15-km grid across central California, assuming that deformation within each grid box is homogenous. The α-angles are then contoured across the region (Fig. 10b).

Oblique convergence angles vary significantly along-strike and, to a lesser extent, across the fault system. In the northwest portion of the San Andreas fault, α-angles are generally $<30^{\circ}$, whereas in the southeast portion, α-angles increase to up to 60°. Across-fault variation includes a region of 75° obliquity that is adjacent to the central section of the fault but predominantly on the southwest side. On the northeast side of the fault, obliquity increases to 90° away from the fault. Along the Rinconada fault, α-angles are generally symmetric across the fault trace but increase southward along-strike.

The magnitude of bulk rotation can also be estimated from each deformation matrix (McKenzie and Jackson, 1983). This is a mathematical value that can be compared to paleomagnetic vertical axis rotations. These bulk rotations are also computed for the gridded region and contoured on a map (Fig. 10c). Local mean rotations from the paleomagnetic data of this study are superimposed for comparison. Because the predicted rotations reflect the spatial distribution and degree of development of regional folds, the largest rotations are predicted northeast of the San Andreas fault and along the Rinconada fault, while no rotation is predicted between these two areas. Predicted

rotations are consistently clockwise but vary in magnitude from 2º-10º along the trace of the Rinconada fault.

The local mean paleomagnetic rotations from this study are mostly consistent with the predicted rotations from folds. For example, the moderate clockwise rotations southwest of the Rinconada fault in the Lockwood subgroup are comparable to the moderate rotations predicted by the fold data. Further, the local mean vector showing no rotation nearest the San Andreas fault is consistent with the absence of folds indicating no predicted rotation. What are not consistent, though, are the regions with counterclockwise paleomagnetic rotation vectors; these fall in an area where the fold data predict small (4º-6º) of clockwise rotations. However, this kinematic fold model can only predict clockwise rotations, so I suggest that these data sets are generally consistent for central California.

Short-term deformation data

The GPS velocity field was used to document patterns of short-term deformation in central California. Figure 11a shows GPS velocities corrected for the plate motion on which the stations are located. Thus, sites northeast of the San Andreas fault have had the motion of the Sierra Nevada-Great Valley block removed from their velocities. Similarly, sites southwest of the San Andreas fault have had Pacific plate motion removed. Note that this unusual way to show GPS data results in a velocity field that is "backwards" from the normal reference used for plate boundaries; normally, we think of motion relative to the adjacent place, not motion at a particular point (in this case, a GPS station) relative to the plate on which that point lies. However, this atypical system of using two reference frames is the only way to accurately show off-fault deformation with along-

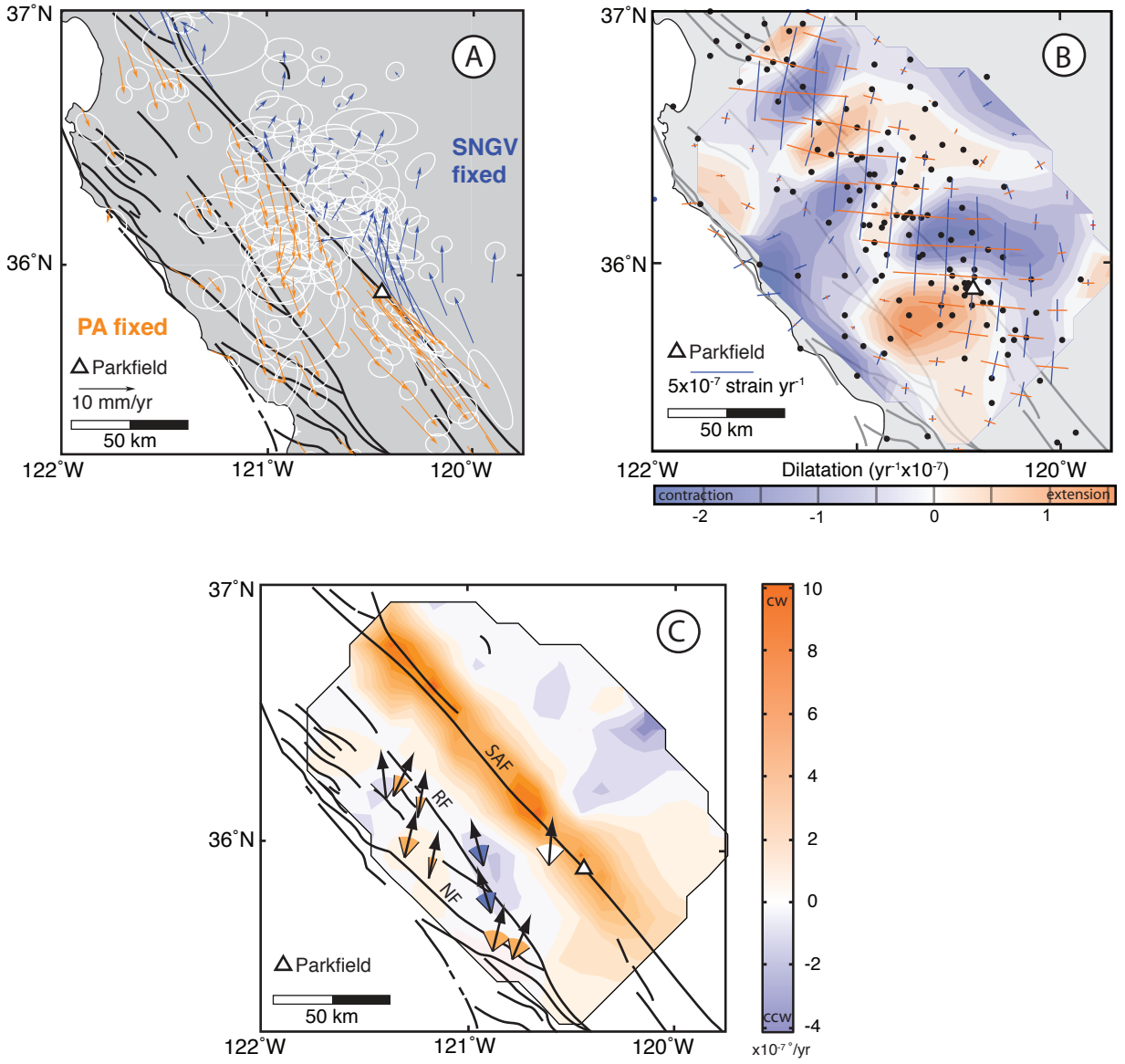

Figure 11. Maps of central California with data based on the GPS velocity field. A.) GPS velocity vectors with two reference frames: southwest of the San Andreas fault, vectors are relative to a stable Pacific (PA) plate; northeast of the fault, vectors are relative to a stable Sierra Nevada-Great Valley (SNGV) microplate. See text for further explanation. B.) Contoured plot of dilitation rates; instantaneous stretching axes (blue lines = principal shortening, orange lines = principal extension), GPS stations (black dots), and major faults are also shown. C.) Contoured plot of rotation rates predicted from the velocity field; paleomagnetic local mean rotations are superimposed, with error wedges colored with the same rotation-based color scheme as the contoured plot. SAF = San Andreas fault; RF = Rinconada fault; NF = Nacimiento fault. Modified from Titus et al. (in review).

strike variation due to changes in fault behavior. This results in an unusual depiction of the velocity field in Figure 11a, in which the San Andreas fault appears to have a sinistral sense of motion, and the locked section has faster velocity vectors than the creeping section. The kinematic results of the velocity field are the same regardless of the reference system used, so I will use the two-reference-frame system for this analysis.

The city of Parkfield (represented by a white triangle in Fig. 11a-c) roughly marks the transition from locked to creeping behavior for the San Andreas fault. This transition is clearly reflected in the velocity field. For sites northeast of the San Andreas fault, those adjacent to the locked segment are faster and nearly parallel to the fault, whereas sites adjacent to the creeping segment are slower and N- to NNE-directed (nearly perpendicular to the strike of the fault). This pattern is similar on the southwest side of the fault: sites adjacent to the locked segment are faster and nearly parallel to the fault, while sites adjacent to the creeping segment are slower and S- to SSE-directed.

From the velocity field, Titus et al. (in review) calculate dilatation rates across the region based on the method of Allmendinger et al. (2007). Figure 11b shows contoured dilatation rates highlighting regions of positive dilatation (extension) and negative dilatation (contraction). The most notable features in this data set occur on either side of the San Andreas fault at the locked-to-creeping transition near Parkfield. Northwest of Parkfield, the model predicts a region of contraction, which is caused by the faster motion of sites adjacent to the locked section relative to sites adjacent to the creeping section. Similarly, a region of extension southwest of the fault is caused by the slower motion of sites adjacent to the creeping section relative to sites adjacent to the locked section. Note

that this region of extension includes a portion of the rocks adjacent to the Rinconada fault that were analyzed in this study.

The rotational component of the GPS velocity field can be computed from the vorticity matrix, as described in more detail in McKenzie and Jackson (1983). These short-term rotations are contoured on a map in Figure 11c as rotation rates, with the local mean paleomagnetic rotations from this study superimposed for comparison. The largest clockwise rotations are predicted along the San Andreas fault, and rotations decrease with distance from the fault symmetrically. Near the Rinconada fault, rotations are much smaller, in part due to the fewer number of GPS stations, but also because the Rinconada fault is less important than the San Andreas fault for accommodating relative plate motion. The most surprising pattern is the region of counterclockwise rotations along the central stretch of the Rinconada fault.

The paleomagnetic rotations are consistent with several aspects of the rotations predicted from the velocity field. Perhaps most noteworthy is that the two moderate counterclockwise paleomagnetic rotations coincide with the region of counterclockwise rotations predicted from the velocity field. Also, clockwise paleomagnetic rotations in the central portion of the study area are consistent with the clockwise rotation rates predicted by the GPS data. The one paleomagnetic rotation that does not fit this model is the local mean from nearest the San Andreas fault—the paleomagnetic data predict no rotation whereas the velocity field predicts large clockwise rotations.

DISCUSSION

Comparison with other paleomagnetic data

The overall mean rotation from 58 sites along the Rinconada fault of 8.4º ± 7.9º is slightly less than was reported by previous paleomagnetic studies conducted along the Rinconada fault. Data from 11 sites within our 58-site data set indicated 14 ± 7º (Titus et al., 2007). Omarzai (1996) reported a rotation of 14.4 ±5º within the Arroyo Seco subgroup of this study (Fig. 1). Given the specific location of data collection for these two sites, however, they are more readily reconciled with the rotations that increase systematically up to ~25º in the Arroyo Seco subgroup. The extensive data collection of this study offers new, higher-resolution information on the spatial distribution of rotation along much of the Rinconada fault.

In this discussion, I will address the kinematics and geometry of vertical axis rotations, the insights offered by two other predictors of rotation, and the implications of off-fault deformation for seismic forecasting.

Kinematics and block geometry

Kinematic models that explain vertical axis rotation are important for understanding how off-fault deformation in central California fits into larger deformation models. These deformation models are important for characterizing transform plate boundaries with specific applications such as forecasting seismicity in various regions across the fault system. Therefore, I attempt to fit the paleomagnetic rotations from this study into vertical axis rotation models from previous studies.

Previous models have been used to explain vertical axis rotation in terms of size of blocks and kinematics of rotation. For example, a kinematic model for the western Transverse Ranges assumes that rotation occurs on internally rigid elongate crustal blocks bound on the surface by vertical strike-slip faults (Luyendyk et al., 1980;

Hornafius et al., 1986). This model is comparable to the “domino block” model of McKenzie and Jackson (1983), in which parallel elongate blocks rotate between major bounding faults and minor conjugate faults (Fig. 12). This type of rotation requires both dextral and sinistral motion on the bounding faults, which works well in the western Transverse Ranges given the conjugate strike-slip faults found in this area. This large-block model is also supported by the consistency of paleomagnetic rotations across regions tens to hundreds of meters across, indicating large rotational domains.

Other kinematic models for block rotation rely on smaller deforming blocks. Beck (1976) proposed the “ball bearing” hypothesis in which small blocks, approximated as circles, rotate and translate northward between bounding faults. This model implies that the blocks are roughly the width of the shear zone and predicts that rotations should be consistent both along-strike and perpendicular to the fault.

These block models do not adequately describe rotations along the Rinconada fault. The significant spatial gradients within relatively small sections of our study area indicate that rotation occurred on smaller units than the blocks from the western Transverse Ranges. Further, the conjugate bounding strike-slip faults necessary for the western Transverse Ranges or domino block models are not present in the Rinconada fault zone. The ball bearing model also cannot fully explain rotation along the Rinconada fault; variations in rotations both along-strike and perpendicular to the fault do not fit with the consistent rotations predicted by the ball bearing hypothesis.

A “quasi-continuum” rotation model from Sonder et al. (1994), in which blocks are small (2-4 km) and irregularly shaped (Fig. 12), may be more appropriate for data from central California. This model predicts a gradient of rotation perpendicular to the

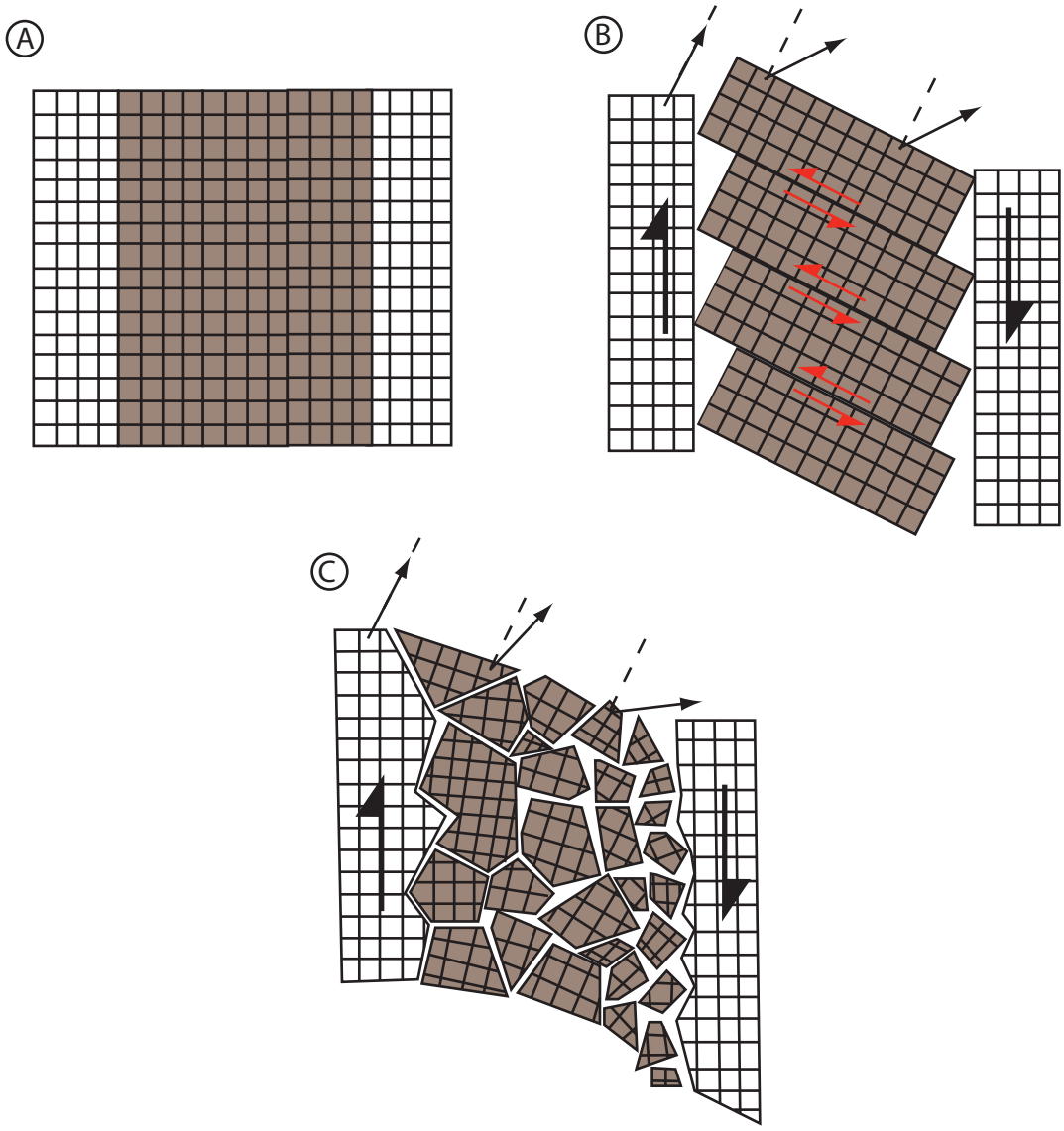

Figure 12. Diagram of block models with large arrows indicating sense of motion across a shear zone and small black arrows indicating paleomagnetic rotations relative to dotted line. A.) Undeformed blocks. B.) Domino block model from McKenzie and Jackson (1983) in which large blocks rotate uniformly. Motion is facilitated by sinistral faults (represented by red arrows), and rotations are consistent across the shear zone. C.) Quasi-continuum model in which small, irregular blocks rotate differentially. Rotations are expected to increase with proximity to the fault; in this case, rotations increase left-to-right. Modified from Sonder et al. (1994).

strike of the fault, as observed in the Arroyo Seco data, and calls upon rotation controlled by rheology of the upper crust, length of the shear zone, and total offset (Sonder et al., 1994). Because variation indicates small rotating units and because of a strong rotational gradient perpendicular to the fault in the Arroyo Seco subgroup, this quasi-continuum model is probably the best approximation of rotation along the Rinconada fault.

Comparison with other deformation data sets

Even the quasi-continuum model, however, cannot account for the along-strike variation in paleomagnetic rotations from the Rinconada fault. This variation is probably a result of the unique tectonic and geologic conditions of the region. I propose that the insights gained from predicted rotations from fold modeling and GPS data can better explain the spatial distribution of rotations along the Rinconada fault. Each data set predicts some aspect of the observed rotations, and combining insight from each leads to a more integrated understanding of off-fault deformation.

Rotations calculated from mapped fold data are consistent with most of the paleomagnetic rotations from this study, where clockwise rotations are observed along most of the Rinconada fault and no rotation is observed southwest of the San Andreas fault. In this region between the Rinconada and San Andreas faults, a notable absence of folds is observed (Fig. 10a). This asymmetry in off-fault deformation along the San Andreas fault in this region is probably controlled, in part, by basement rock type: Salinian basement southwest of the San Andreas fault is more competent and therefore less deformable compared to the Franciscan basement northeast of the fault. The absence of vertical axis rotation southwest of the San Andreas fault, which is observed in paleomagnetic rotations from this study and predicted by rotations computed from fold

data, is consistent with this explanation of basement rock control. Indeed, previous studies document rotation in the less-competent Franciscan region northeast of the fault. Paleomagnetic data from White (1987) indicate 12 ± 2º of clockwise rotation in Kettleman Hills (Fig. 1), and well log data from Julander (1992) show ~24º of clockwise rotation in the Lost Hills. Thus, basement rock type is probably an important control in off-fault deformation in central California.

The one major inconsistency between the paleomagnetic rotations from this study and rotations predicted by the map data is in the region with counterclockwise paleomagnetic rotations. However, the mathematical model used to compute rotations from mapped fold data can only predict clockwise rotations. Within the limitations of this model, general agreement between paleomagnetic rotations and fold data predictions provide confidence in results and important insight into the role of basement rock in controlling distributed deformation.

The paleomagnetic rotations from this study are also generally consistent with bulk rotation calculated from the GPS velocity field. Perhaps most surprisingly, moderate counterclockwise paleomagnetic rotations in the Lockwood and San Antonio Reservoir subgroups fit perfectly within a region of counterclockwise rotation predicted by the velocity field (Fig. 11c). Normally, counterclockwise rotation would never be expected in a dextral strike-slip regime. However, the velocity field may offer an explanation for this anomalous rotation. This region is adjacent to the creeping-to-locked transition on the San Andreas fault, and the velocity field reflects this change in fault behavior. Specifically, the shift in the velocity vectors from southeast-directed (roughly fault-parallel) adjacent to the locked section to more south-directed (oblique to the fault)

adjacent to the creeping section create the kinematic conditions necessary for counterclockwise rotation (Fig. 13). Through time, relatively competent blocks adjacent to the locked and creeping segments move apart in the fault-parallel direction and offset in the fault-perpendicular region, theoretically resulting in a basin that experiences counterclockwise rotation. One important implication of this finding is that if counterclockwise rotations are indeed related to the creeping-to-locked transition, the paleomagnetic data from this study suggest that the creeping segment may have been aseismic over geologic time scales.

It is difficult to estimate when creeping behavior along the San Andreas fault began. However, the changing velocity vectors due to the creeping-to-locked transition allow a back-of-the-envelope calculation based on Figure 13. The kinematics of two major crustal blocks are predicted from the average GPS velocity of each block relative to the stable Pacific plate. The block adjacent to the locked section moves faster and in a nearly fault-parallel direction, while the block adjacent to the creeping segment moves more slowly and oblique to the fault. Through time, this difference should result in a basin that has a left-lateral geometry. By using reasonable velocities for the two blocks, I can approximate the shape of this resultant basin after each million-year time step. The specific geometry of the basin should result in a predictable rate of counterclockwise rotation of rocks within the area.

For this transtensional basin, I use the transpression/transtension matrix from Fossen and Tikoff (1993) to determine γ, the shear strain; the predicted rotation due to this shear strain is simply $\gamma/2$ (McKenzie and Jackson, 1983). This estimate suggests a counterclockwise rotation rate of about ~10º/m.y. for the extensional region between the

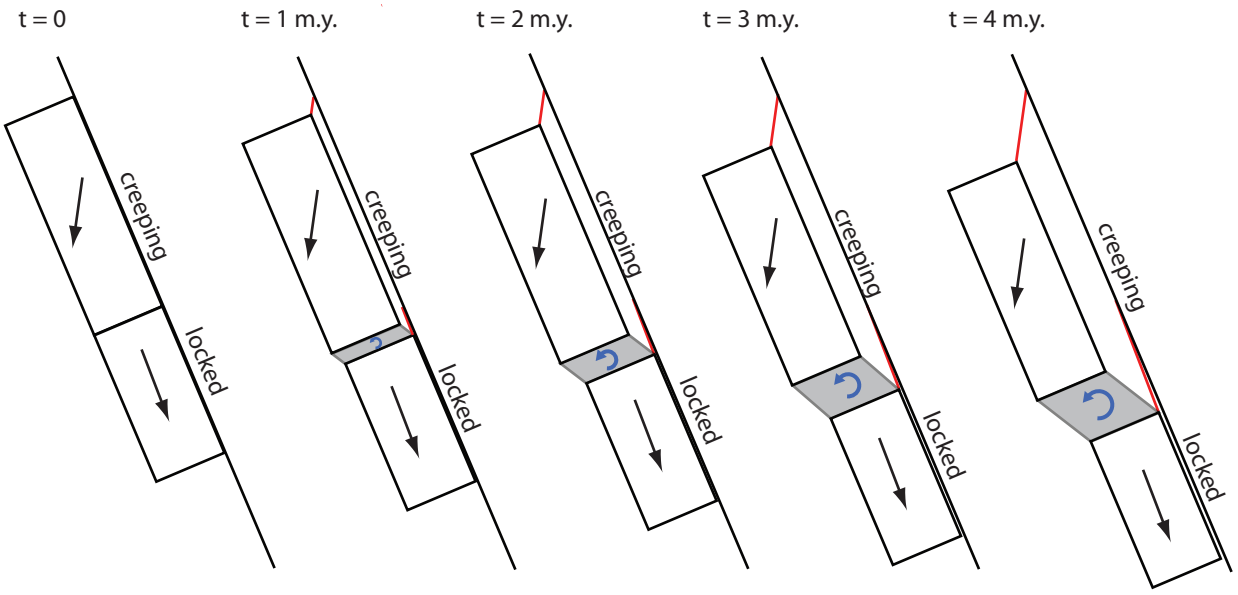

Figure 13. Schematic depiction of the southwest side of the San Andreas fault including the locked-to-creeping transition. The kinematics of two major crustal blocks are predicted from the average GPS velocity of each block relative to the stable Pacific plate, shown by black arrows as rates in km/3 m.y. Red lines mark the total offset of each block from its original position for each million-year time step. Through time, the different velocities for the two blocks should result in a basin, shown in gray, that has left-lateral geometry. This geometry would cause counterclockwise rotations of rocks within the area, represented by blue arrows. Paleomagnetic data from this study show moderate counterclockwise rotation in this region.

blocks. The local mean rotations from paleomagnetic data suggest 17.5 ± 30.8º and 15.0 ± 28.4º of counterclockwise rotations within this extensional region (Fig. 11c). Because some amount of clockwise rotation probably occurred in the rocks recording paleomagnetic data before creeping behavior along the San Andreas fault began, a counterclockwise rotation rate of 10º/m.y. (which I propose is associated with creeping fault behavior) would result in ~15º of counterclockwise net rotation in a few million years. Thus, the GPS velocity field provides novel insights into anomalous rotations possibly associated with the creeping behavior of the San Andreas fault and suggests that such fault behavior has been active on geologic time scales.

One prominent exception to agreement between the paleomagnetic rotations and rotations predicted from the GPS velocity field is in the local mean rotation nearest the San Andreas fault. The paleomagnetic data here show no appreciable rotation, while rotations predicted by the velocity field show moderate clockwise rotation in this region. The GPS calculations, however, assume that the same material is found on either side of the San Andreas fault; thus, its rotation model predicts evenly distributed rotation across the fault. As discussed above, the competency of the Salinian basement actually results in little deformation southwest of the San Andreas. Still, this limitation of the velocity field model does not prevent meaningful comparison with the paleomagnetic data in other parts of the study area, especially in the region of counterclockwise rotations where the importance of fault behavior can be discerned.

Taken together, these independent data sets from folds and GPS velocity field provide meaningful insight into the mechanisms behind the spatial distribution of paleomagnetic rotations in central California. Both data sets are consistent with moderate

amounts of clockwise rotations along much of the Rinconada fault; the fold data show how the competent Salinian block may have resulted in no rotations on the southwest side of the San Andreas fault; and the GPS velocity field demonstrates how the locked-to-creeping transition may have resulted in moderate counterclockwise rotations in an isolated region along the Rinconada fault.

Implications for seismic forecasting

The rotations from paleomagnetic data and those predicted from fold and GPS data provide information about the distribution of plate boundary deformation, which is important for characterizing seismic hazards in central California. Seismic forecasting depends, in part, on long-term slip rates to calculate probable recurrence intervals for characteristic earthquakes. Figure 14 is a probabilistic seismic hazard map for California, which shows that the region adjacent to the creeping segment is assigned a low probability for significant earthquake activity. However, traditional models, including that which was used for this seismic hazard map, assume that almost all relative plate motion is taken up on the San Andreas fault. Bird (2009) shows that long-term seismicity can be calculated more accurately with models that account for off-fault deformation and high-resolution spatial variability in slip rates. His models produce slip rates for the western United States that are slower than previously calculated because they account for permanent distributed deformation, which takes up approximately one third of relative plate motion in California.

Calculations of seismic hazard in central California typically use a slip rate of ~34 mm/yr for the San Andreas fault (e.g., Savage and Burford, 1970; Lisowski et al., 1991; Argus and Gordon, 2001) based on the assumption that slip rates should match the long-

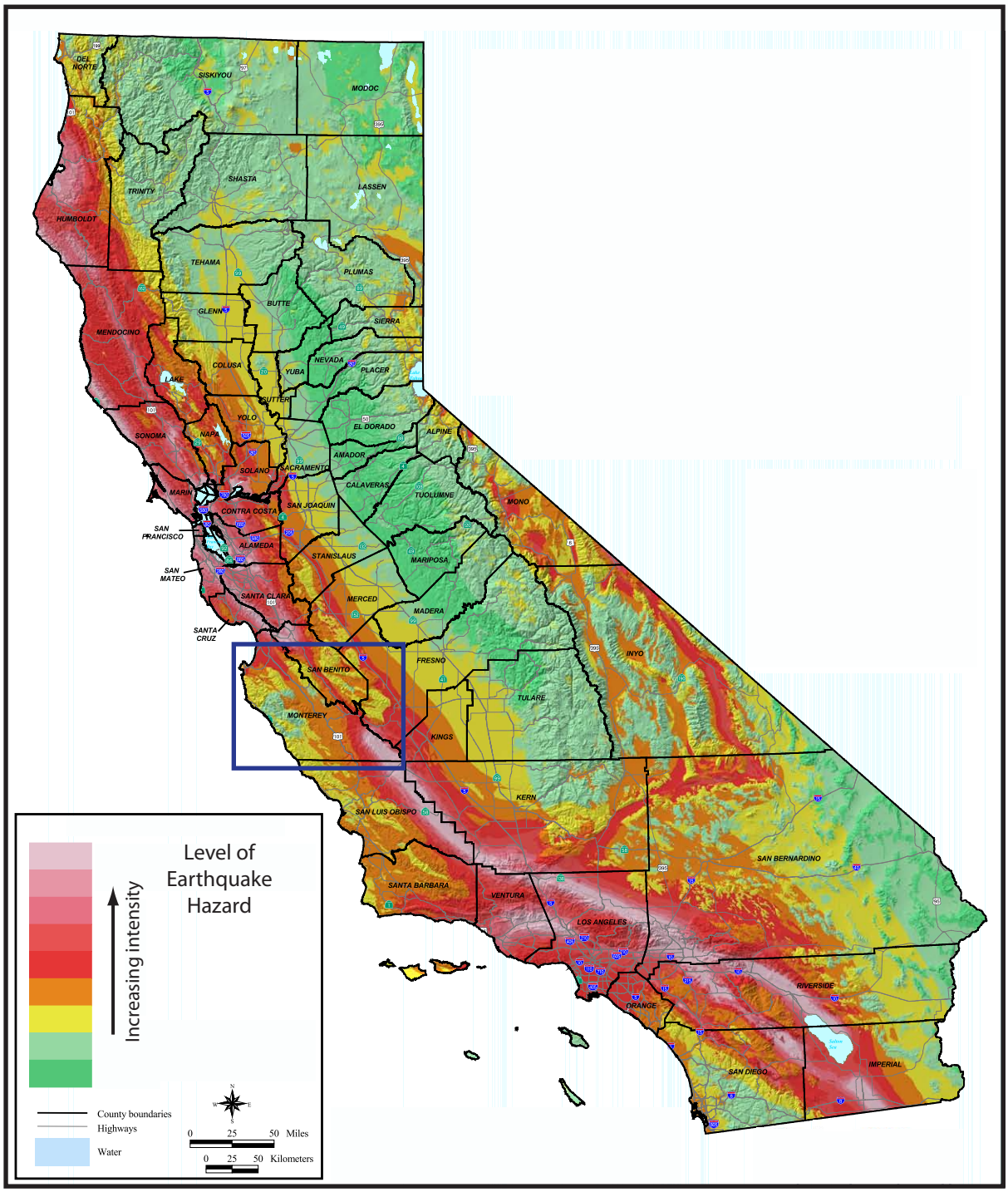

Figure 14. Seismic hazard map for the state of California, with the study area highlighted by a blue box. Note that the creeping segment of the San Andreas fault has a much lower probability of major earthquake activity than the rest of the fault, which is locked. The borderlands of the fault in central California have an even lower probabilistic seismic hazard; however, this may be an underestimation, as models used in forecasting seismicity do not account for the potential seismicity due to off-fault deformation. Modified from Frankel et al. (2002).

term geologic slip rate (Sieh and Jahns, 1984). This rate is a large fraction of the total 37-39 mm/yr expected between the Sierra Nevada – Great Valley microplate and the Pacific plate (Argus and Gordon, 2001). These calculations of slip rate do not estimate or account for off-fault deformation. However, more recent work in central California suggests that the slip rate along the San Andreas fault is significantly slower: Titus et al. (2006) determine a rate of 28-30 mm/yr from near-fault geodetic data, and Bird (2009) estimates a rate of 31.5 mm/yr from modeling various geologic and geodetic data sets. These slower rates indicate that 2.5-12 mm/yr of the fault-parallel plate motion must be distributed in the fault borderlands. Some of this missing slip is taken up in other strike-slip faults in the San Andreas fault system: Bird (2009) estimates slip rates of 1.6 mm/yr for the San Gregorio-Hosgri fault and 0.9 mm/yr for the Rinconada fault. However, ~3-8 mm/yr are still missing from total fault-parallel plate motion. This discrepancy can be resolved by accounting for permanent distributed deformation (Titus et al., 2006; Bird, 2009) (Fig. 15).

Slower San Andreas fault slip rates that account for off-fault deformation, such as rates estimated by Titus et al. (2005) and Bird (2009), are better for computing seismic hazards in that they better recognize the potential for seismicity away from the main strike-slip faults. While current forecasting methods assume that all significant seismicity occurs on the main faults in the San Andreas fault system, historic earthquakes that are not located on mapped faults demonstrate that this is an inaccurate assumption. For example, a set of three moderate earthquakes—the 1982 New Idria, 1983 Coalinga, and 1985 Kettleman Hills earthquakes—occurred on blind thrust faults northeast of the creeping segment of the San Andreas fault (Stein et al., 1992) (Fig. 2). More recently, the 2003 San Simeon earthquake occurred outboard of the Rinconada fault (Hauksson et al.,

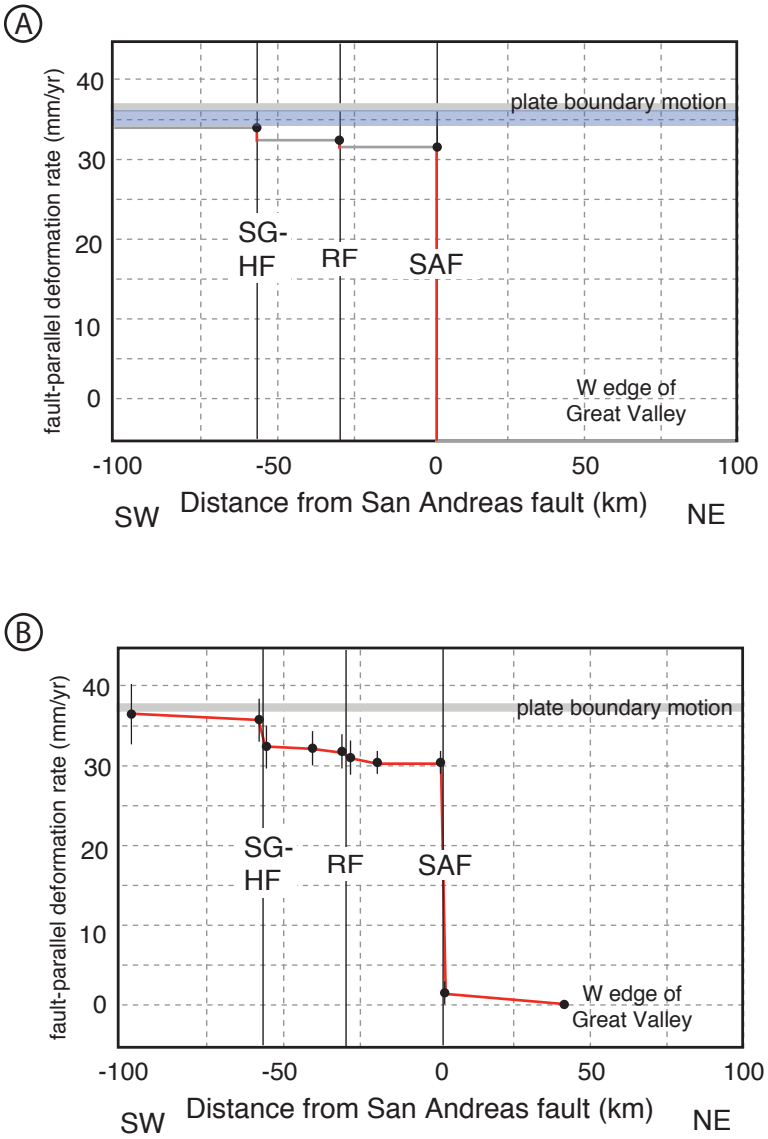

Figure 15. Diagram depicting summation of fault-parallel components of plate motion across central California. A) Summation of discrete offsets (vertical red lines) on the San Andreas fault (SAF), Rinconada fault (RF), and San Gregorio-Hosgri fault (SG-HF). These offsets do not add up to the total plate boundary motion (thick gray line); this missing slip is shaded in blue. Slip rates on the three faults and fault-parallel component of plate motion are from Bird (2009) (see text). B) Summation of discrete offsets and off-fault deformation, with each dot representing cumulative deformation across a given region, based on Titus et al. (in review). Note that when off-fault deformation is accounted for, total fault-parallel motion across the San Andreas fault system add up to the expected fault-parallel component of relative plate motion. Modified from Titus et al. (in review).

2004). These damaging earthquakes reveal that off-fault deformation may result in earthquakes, and accurate probabilistic seismic hazard calculations must consider distributed deformation in order to correctly forecast seismicity in the fault borderlands. Current seismic forecasts, such as the one in Figure 14, may underestimate earthquake potential in the borderlands of central California, away from major strike-slip faults. Quantifying vertical axis rotations along the Rinconada fault is an important component of understanding off-fault deformation in central California, where destructive seismicity has occurred.

CONCLUSIONS

Paleomagnetic data was collected from 177 sites along the Rinconada fault in central California in order to quantify vertical axis rotations in the fault borderlands. Of the 58 statistically viable sites, the average clockwise rotation is 8.4º ± 7.9º since the mid-Miocene. However, the magnitude of vertical axis rotations varies along and across the fault, including clockwise rotations up to 25º, regions with no appreciable rotation, and even an isolated region of moderate counterclockwise rotation.

The inconsistency of rotations across relatively small areas and the apparent absence of conjugate bounding faults indicate that the rotating blocks in this region cannot be described according to most traditional vertical axis rotation models, including the large-block model of the Western Transverse Ranges to the south. A better model for the kinematics of rotation in this region is the quasi-continuum model presented by Sonder et al. (1994), in which small, irregularly shaped blocks rotate differentially across the shear zone, but even this model cannot predict the variations in vertical axis rotations

along the Rinconada fault. GPS and fold data, however, shed light on this pattern and provide important information on the kinematics and style of distributed deformation.

The paleomagnetic results are largely consistent with two independent predictors of rotation in the borderland. Rotations calculated from the distribution, orientation, and magnitude of mapped folds predict changing clockwise rotation along the Rinconada fault and a region of no rotation on the southwest side of the San Andreas fault, likely the result of the competent Salinian basement in this region resisting permanent deformation. Rotations calculated from the GPS velocity field show isolated regions of counterclockwise rotations, which would normally not be expected in a dextral setting but are consistent with our anomalous counterclockwise rotations from paleomagnetic data in this study. Because the velocity field appears to be controlled by the locked-to-creeping transition on the San Andreas fault, these counterclockwise rotations may be caused by long-term creep along the San Andreas fault over geologic time scales.

While the paleomagnetic rotations along the Rinconada fault are smaller than in other regions of the San Andreas fault system, they represent an example of the importance of documenting off-fault deformation. Characterizing distributed permanent deformation is essential in creating accurate kinematic models of fault zones and in forecasting seismicity. Off-fault deformation, including vertical axis rotation in the fault borderlands, must be incorporated into models of the San Andreas fault and other fault zones to improve our understanding of plate boundary deformation.

ACKNOWLEDGMENTS

I would like to sincerely thank Sarah Titus for helping with every aspect of this project—from envisioning and initiating this study to endless help in the writing process. I am grateful to all those who assisted in collecting paleomagnetic cores from 2004-2008: Bernie Housen, Eric Horsman, Basil Tikoff, Sarah Titus, Zack McGuire, and Paul Riley. I thank Bernard Housen and Russell Burmester at Western Washington University for extensive assistance in paleomagnetic analysis. I am grateful to Eric Horsman for generating geologic maps with paleomagnetic stations located. I extend a special thanks to Mark Dyson for his computer modeling of rotations predicted from fold data and the GPS velocity field. I thank Liz Anderson for helpful text editing. Finally, thank you to the Carleton College Geology Department and my fellow majors for support throughout the course of this project. This study was funded by a Petroleum Research Fund grant to Sarah Titus.

REFERENCES CITED

Aagaard, B., Barall, M., Brocher, T. M., Dolenc, D., Dreger, D., Graves, R. W., Harmsen, S., Hartzell, S., Larsen, S., McCandless, K., Nilsson, S., Petersson, N. A., Rodgers, A., Sjogreen, B., and Zoback, M. L., 2009, Data files for ground-motion simulations of the 1906 San Francisco earthquake and scenario earthquakes on the northern San Andreas Fault: U. S. Geological Survey, DS-0413.

Allmendinger, R. W., Reilinger, R., and Loveless, J., 2007, Strain and rotation rate from GPS in Tibet, Anatolia, and the Altiplano: Tectonics, v. 26. p. doi:10.1029/2006/TC002030.

Argus, D. F., and Gordon, R. G., 2001, Present tectonic motion across the Coast Ranges and San Andreas fault system in Central California: Geological Society of America Bulletin, v. 113, p. 1580-1592.

Beck, M. E., 1976, Discordant paleomagnetic pole positions as evidence for regional shear in the western Cordillera of North America: American Journal of Science, v. 276, p. 694-712.

Besse, J., and Courtillot, V., 2002, Apparent and true polar wander and the geometry of the geomagnetic field over the last 200 Myr: Journal of Geophysical Research, v. 107, p.

no.B11, 31.

Bird, P., 2009, Long-term fault slip rates, distributed deformation rates, and forecast of seismicity in the western United States from joint fitting of community geologic, geodetic, and stress direction data sets: Journal of Geophysical Research, v. 114, p. doi:10.1029/2009JB006317

Blake, M. C., Jr., Campbell, R. H., Dibblee, T. W., Jr., Howell, D. G., Nilsen, T. H., Normark, W. R., Vedder, J. G., and Silver, E. A., 1978, Neogene basin formation in relation to plate tectonic evolution of San Andreas fault system, California: AAPG Bulletin, v. 62, p. 344-372.

Boatwright, J., Keefer, D. K., Anderson, J. G., and von Seggern, D. H., 2005, The distribution of violent shaking in the 1906 San Francisco earthquake, Seismological Research Letters: El Cerrito, Seismological Society of America, p. 253-254.

Burford, R. O., and Harsh, P. W., 1980, Slip on the San Andreas Fault in central California from alinement array surveys: Bulletin of the Seismological Society of America, v. 70, p. 1233-1261.

Champion, D. E., Howell, D. G., and Gromme, C. S., 1984, Paleomagnetic and geologic data indicating 2500 km of northward displacement for the Salinian and related terranes, California: Journal of Geophysical Research, v. 89, p. 7736-7752.

d'Alessio, M. A., Johanson, I. A., Buergmann, R., Schmidt, D. A., and Murray, M. H., 2005, Slicing up the San Francisco Bay area; block kinematics and fault slip rates from GPS-derived surface velocities: Journal of Geophysical Research, v. 110, p. no.B5, 19.

Demarest, H. H., Jr., 1983, Error analysis for the determination of tectonic rotation from paleomagnetic data: Journal of Geophysical Research, v. 88, p. 4321-4328.

Dibblee, T. W., Jr., 1976, The Rinconada and related faults in the southern Coast Ranges, California, and their tectonic significance: U. S. Geological Survey, P 0981.

Ellis, B. J., 1994, Changing tectonic regimes in the southern Salinian Block; extension, strike-slip faulting, compression and rotation in the Cuyama Valley, California [Doctoral thesis]: Oregon State University.

Fossen, H., and Tikoff, B., 1993, The deformation matrix for simultaneous simple shearing, pure shearing and volume change, and its application to transpression-transtension tectonics: Journal of Structural Geology, v. 15, p. 413-422.

Frankel, A. D., Peterson, M. D., Muller, C. S., Haller, K. M., Wheeler, R. L., and Leyendecker, K. S., 2002, Documentation for the 2002 Update of the National Seismic Hazard Maps.

Greenhaus, M. R., and Cox, A., 1979, Paleomagnetism of the Morro Rock-Islay Hill complex as

evidence for crustal block rotations in central coastal California: fault mechanics: Journal of Geophysical Research, v. 84, p. 2393-2400.

Hauksson, E., Oppenheimer, D., and Brocher, T. M., 2004, Imaging the source region of the 2003 San Simeon earthquake within the weak Franciscan subduction complex, central California: Geophysical Research Letters, v. 31.

Hill, M. L., and Dibblee, T. W., Jr., 1953, San Andreas, Garlock, and Big Pine faults, California; a study of the character, history, and tectonic significance of their displacements: Geological Society of America Bulletin, v. 64, p. 443-458.

Holm, E. J., Horns, D. M., and Verosub, K. L., 1991, Rapid post-Miocene tectonic rotation associated with the San Gregorio fault zone in Central California: Geophysical Research Letters, v. 18, p. 2213-2216.

Hornafius, J. S., 1985, Neogene tectonic rotation of the Santa Ynez Range, western Transverse Ranges, California, suggested by paleomagnetic investigation of the Monterey Formation: Journal of Geophysical Research, v. 90, p. 12,503-12,522.

Hornafius, J. S., Luyendyk, B. P., Terres, R. R., and Kamerling, M. J., 1986, Timing and extent of Neogene tectonic rotation in the western Transverse Ranges, California: Geological Society of America Bulletin, v. 97, p. 1476-1487.

Hornafius, J. S., Luyendyk, B. P., Weaver, D. W., Wornardt, W. W., Fuller, M., and Anonymous, 1981, Paleomagnetic results from the Monterey Formation in the western Transverse Ranges, California, Eos, Transactions, American Geophysical Union: Washington, American Geophysical Union, p. 855.

Horns, D. M., and Verosub, K. L., 1995, Paleomagnetic investigation of late Neogene vertical axis rotation and remagnetization in central coastal California: Journal of Geophysical Research, v. 100, p. 3873-3884.

Isaacs, C. M., 1980, Diagenesis in the Monterey Formation examined laterally along the coast near Santa Barbara, California: U. S. Geological Survey, OF 80-606.

Julander, D. R., 1992, Implications from a study of the timing of oil entrapment in Monterey siliceous shales, Lost Hills, San Joaquin Valley, California, 1992 annual meeting of the Geological Society of America (GSA): Cincinnati, OH, Geological Society of America, Abstracts with Programs.

Lisowski, M., Savage, J. C., and Prescott, W. H., 1991, The velocity field along the San Andreas Fault in Central and Southern California: Journal of Geophysical Research, v. 96, p. 8369-8389.

Luyendyk, B. P., Kamerling, M. J., and Terres, R., 1980, Geometric model for Neogene crustal rotations in southern California: Geological Society of America Bulletin, v. 91, p. 211-

217.

Luyendyk, B. P., Kamerling, M. J., Terres, R. R., and Hornafius, J. S., 1985, Simple shear of Southern California during Neogene time suggested by paleomagnetic declinations: Journal of Geophysical Research, v. 90, p. 12,454-12,466.

McKenzie, D., and Jackson, J., 1983, The relationship between strain rates, crustal thickening, palaeomagnetism, finite strain and fault movements within a deforming zone: Earth and Planetary Science Letters, v. 65, p. 182-202.

Olsen, A. H., Aagaard, B. T., Heaton, T. H., and Beroza, G. C., 2008, Long-period building response to earthquakes in the San Francisco Bay area: Bulletin of the Seismological Society of America, v. 98, p. 1047-1065.

Omarzai, S. K., 1996, Paleomagnetism Applied to the Monterey Formation of California [Ph.D. thesis]: University of California Santa Cruz, 220 p.

Onderdonk, N. W., 2005, Structures that accommodated differential vertical axis rotation of the western Transverse Ranges, California: Tectonics, v. 24, p. no.4, 15.

Page, B. M., Thompson, G. A., and Coleman, R. C., 1998, Late Cenozoic tectonics of the central and southern Coast Ranges of California: Geological Society of America Bulletin, v. 110, p. 846-876.

Rolandone, F., Buergmann, R., Agnew, D. C., Johanson, I. A., Templeton, D. C., d'Alessio, M. A., Titus, S. J., DeMets, C., and Tikoff, B., 2008, Aseismic slip and fault-normal strain along the central creeping section of the San Andreas Fault: Geophysical Research Letters, v. 35.

Rubinstein, J. L., and Beroza, G. C., 2004, Evidence for widespread nonlinear strong ground motion in the M (sub W) 6.9 Loma Prieta earthquake: Bulletin of the Seismological Society of America, v. 94, p. 1595-1608.

Savage, J. C., and Burford, R. O., 1970, Accumulation of tectonic strain in California: Bulletin of the Seismological Society of America, v. 60, p. 1877-1896.

Sieh, K. E., and Jahns, R. H., 1984, Holocene activity of the San Andreas Fault at Wallace Creek, California: Geological Society of America Bulletin, v. 95, p. 883-896.

Sonder, L. J., Jones, C. H., Salyards, S. L., and Murphy, K. M., 1994, Vertical axis rotation in the Las Vegas Valley Shear Zone, southern Nevada: Paleomagnetic constraints on kinematics and dynamics of block rotations: Tectonics, v. 13, p. 769-788.

Stein, R. S., Eaton, J. P., and Eberhart-Phillips, D., 1992, Seismicity and geometry of a 110-km-long blind thrust fault: Journal of Geophysical Research, v. 97, p. 4843-4864.

Tauxe, L., and Watson, G. S., 1994, The fold test: an eigen analysis approach: Earth and Planetary Science Letters, v. 122, p. 331-341.

Titus, S. J., DeMets, C., and Tikoff, B., 2005, New slip rate estimates for the creeping segment of the San Andreas Fault, California: Geology, v. 20, p. 661-672.

Titus, S. J., DeMets, C., and Tikoff, B., 2006, Thirty-five-year creep rates for the creeping segment of the San Andreas Fault and the effects of the 2004 Parkfield earthquake; constraints from alignment arrays, continuous Global Positioning System, and creepmeters, Bulletin of the Seismological Society of America, S250-S268 p.

Titus, S. J., Dyson, M., DeMets, C., Tikoff, B., Rolandone, F., and Buergmann, R., in review, Geologic versus geodetic deformation adjacent to the San Andreas fault, central California: Geological Society of America Bulletin.

Titus, S. J., Housen, B., and Tikoff, B., 2007, A kinematic model for the Rinconada fault system in central California based on structural analysis of en echelon folds and paleomagnetism: Journal of Structural Geology, v. 29, p. 961-982.

Twiss, R. J., and Unruh, J. R., 2007, Structure, deformation, and strength of the Loma Prieta fault, northern California, USA, as inferred from the 1989-1990 Loma Prieta aftershock sequence: Geological Society of America Bulletin, v. 119, p. 1079-1106.

Wells, R. E., 2004, The Loma Prieta, California, earthquake of October 17, 1989; geologic setting and crustal structure; introduction: U. S. Geological Survey, P 1550-E.

White, R., 1987, Paleomagnetism of the Tulare Formation from cores and surface exposures, west-central and southwestern San Joaquin Valley [Master's thesis]: California State University at Long Beach.

Zijderveld, J. D. A., 1967, A.C. demagnetization of rocks: analysis of results., *in* Creer, K. M., and Runcorn, S. K., eds., Methods in Paleomagnetism: New York, Elsevier, p. 254-286.